

RESEARCH ARTICLE

Observed patterns of surface solar irradiance under cloudy and clear-sky conditions

Wouter Mol  | Bert Heusinkveld  | Mary Rose Mangan  | Oscar Hartogensis  |
Menno Veerman  | Chiel van Heerwaarden 

Meteorology and Air Quality Group,
Wageningen University, Wageningen,
The Netherlands

Correspondence

Wouter Mol, Meteorology and Air Quality
Group, Wageningen University,
Wageningen, The Netherlands.
Email: wbmol@wur.nl

Funding information

Dutch Research Council (Nederlandse
Organisatie voor Wetenschappelijk
Onderzoek), Grant/Award Number:
VI.Vidi.192.068

Abstract

Surface solar irradiance varies on scales as small as seconds or metres. This variability is driven mostly by wavelength-dependent scattering by clouds, and to a lesser extent by aerosols and water vapour. The highly variable nature of solar irradiance is not resolved by most atmospheric models, yet it affects, most notably, the land–atmosphere coupling and the quality of solar energy forecasting. Characterising variability, understanding the mechanisms, and developing models capable of resolving it accurately requires spatially and spectrally resolved observational datasets of solar irradiance at high resolution, which are rare. In 2021, we deployed a network of low-cost radiometers in the Field Experiment on submesoscale spatio-temporal variability in Lindenberg (FESSTVaL, Germany) and Land surface Interactions with the Atmosphere over the Iberian Semi-arid Environment (LIAISE, Spain) field campaigns to gather data on cloud-driven surface patterns of irradiance, including spectral effects, with the aim of addressing this gap in observations and understanding. We find in case studies of cumulus, altocumulus, and cirrus clouds that these clouds generate large spatiotemporal variability in irradiance, but through different mechanisms and at different spatial scales, ranging from 50 m to 30 km. Spectral irradiance in the visible range varies at similar scales, with significant blue enrichment in cloud shadows, most strongly for cumulus, and red enrichment in irradiance peaks, particularly in the case of semitransparent clouds or near cumulus cloud edges. Under clear-sky conditions, solar irradiance varies significantly in water-vapour absorption bands at the minute scale, due to variability in atmospheric moisture in the boundary layer. With this study, we show that observing detailed spatiotemporal irradiance patterns is possible using a relatively small, low-cost sensor network, and that such network observations can provide insight and validation for the development of models capable of resolving irradiance variability.

KEYWORDS

clouds, local or boundary-layer scale, observations, solar spectral radiation

This is an open access article under the terms of the [Creative Commons Attribution-NonCommercial](https://creativecommons.org/licenses/by-nc/4.0/) License, which permits use, distribution and reproduction in any medium, provided the original work is properly cited and is not used for commercial purposes.

© 2024 The Authors. *Quarterly Journal of the Royal Meteorological Society* published by John Wiley & Sons Ltd on behalf of Royal Meteorological Society.

1 | INTRODUCTION

Solar radiation is a fundamental driver of weather and climate, varying in time and space on a wide range of scales. Variations in solar irradiance at the surface, excluding any influence from vegetation or other obstructions, can occur on scales as small as seconds or tens of metres, and are driven mainly by clouds. Cloud fields generate complex, high-contrast spatial patterns that range from stationary to dynamically evolving, depending on cloud type, cloud velocity, and cloud shape evolution. The spatiotemporal scales of surface irradiance patterns are directly linked to cloud sizes, meaning scales ranging between seconds (10^1 m) and hours (10^5 m) all contribute significantly to the total variance (Mol, van Stratum, et al., 2023; Tabar et al., 2014; Wood & Field, 2011).

Measuring or forecasting these variations is challenging but important to get right, because they influence the coupled land–atmosphere system (i.e., the energy, water, and carbon cycle), atmospheric photochemistry, and solar energy production. For example, heterogeneity in surface heat fluxes driven by cloud-induced irradiance variability can feed back to cloud development (Jakub & Mayer, 2017; Lohou & Patton, 2014; Veerman et al., 2022), and the highly variable nature of solar irradiance negatively impacts electricity grid stability and solar energy yield (Kreuwel et al., 2021; Liang, 2017; Yang et al., 2022). In addition to clouds, light scattering and absorption in the atmosphere by gas molecules and aerosols also result in changes in the light spectrum, which has implications for photosynthesis (Durand et al., 2021) and wavelength-dependent photovoltaic technologies (Dirnberger et al., 2015).

Variability in surface irradiance is amplified by the three-dimensional nature of scattering, and thus redistribution, of solar radiation in the atmosphere. Cloud shadows are caused by the (partial) blocking of direct irradiance and are darker due to part of the light scattering horizontally to an area around the cloud shadow rather than directly in it. When this scattered irradiance combines locally with unobstructed direct irradiance in a cloud-free area, it exceeds clear-sky irradiance and potentially even extraterrestrial irradiance (Cordero et al., 2023; Gueymard, 2017; Yordanov et al., 2015). In this study, we refer to such areas of cloud-induced enhancement of irradiance above clear-sky values as simply “cloud enhancement” (CE), as discussed by Gueymard (2017).

As Earth-system modelling moves to higher resolution and complexity, resolving small-scale variability in irradiance accurately becomes increasingly important, but also more difficult. While the physics of three-dimensional radiative transfer is well-known, the path light takes through an atmosphere filled with liquid water and ice,

aerosols, and gas molecules, and over a partially reflecting surface, is highly complex. To add to the complexity, radiative transfer processes depend on wavelength, in particular in the case of gas absorption (e.g., ozone or water vapour) and Rayleigh scattering, but also clouds become optically more absorbent and sensitive to wavelengths beyond the visible range (O’Hirok & Gautier, 1998; Schmidt et al., 2010). Qualitatively, the spatial patterns of irradiance that a cloudy atmosphere generates can be visible to the eye, for example, from an aerial view or on the side of mountains. However, quantitatively characterising solar spectral irradiance and explaining how exactly it results from a given atmospheric state remains a challenge, especially at small scales.

Both observations and modelling at these small scales have their limitations. Spatial observations of surface irradiance at the scale of cloud shadow and enhancement patterns (10^1 – 10^4 m: (Mol, van Stratum, et al., 2023)), with an adequate temporal resolution of 1 s or better (Tomson, 2010; Yordanov et al., 2013), are rare. Many high-quality solar irradiance observations exist, for example the Baseline Surface Radiation Network (Driemel et al., 2018), but while these adhere to the highest quality standards, they are effectively single-point measurements at typically 1-min resolution. Examples of more dense networks are the 99-pyranometer network deployed during the HD(CP)² Observational Prototype Experiment (Madhavan et al., 2016), or the 17 photodiode pyranometers used by Weigl et al. (2012); Tabar et al. (2014), both deployed on ~ 1 km² scale areas. Photodiode pyranometers are fast-responding ($\ll 1$ s) sensors, and thus capture the fastest atmospheric-driven fluctuations in irradiance, but they do not provide spectral information. None of these networks provides sufficient temporal, spectral, and spatial resolution to characterise surface irradiance heterogeneity at the scale of clouds, in part due to the high cost and operational burden of performing such measurements.

In terms of using modelling, reproducing observed solar-irradiance variability requires a fully resolved and realistic simulation of clouds, information about atmospheric composition and aerosols, and accurate 3D radiative transfer calculations using techniques such as Monte Carlo ray tracing. In practise, the most detailed operational weather models operate at a resolution of approximately 1 km, too coarse to resolve clouds at the necessary scales. Apart from that, the physics of radiative transfer is often simplified to a two-stream approach (up and down: (Hogan & Bozzo, 2018)), which by design means it cannot resolve cloud enhancement and will thus underestimate the contrast between shaded and sunlight surfaces. There are ways to improve upon two-stream methods by subgrid parameterisation of clouds and 3D

radiative effects for operational weather models, such the one introduced by Schäfer et al. (2016) and recently further improved by Ukkonen & Hogan (2024). Resolving 3D radiation more accurately is possible in academic setups, where specific mechanisms can be studied in a controlled manner. For example, Veerman et al. (2022) coupled a 3D Monte Carlo ray tracer to a cloud-resolving model to study cumulus, Gristey et al. (2022) used a similar technique but in an uncoupled setup to study cumulus with aerosol effects, Villefranque et al. (2023) functionalised a ray tracer to study the effect of surface albedo on irradiance in cumulus fields, and Pincus and Evans (2009) demonstrated an alternative to ray tracing altogether. However, even in the best-studied case of boundary-layer shallow cumulus, one can question the realism with which large-eddy simulations (LESs) can resolve such clouds (Romps et al., 2021). This makes validation of irradiance models nontrivial, where errors in irradiance can originate from unrealistic cloud fields rather than from radiative transfer calculations.

Improving parameterised or optimised 3D radiative transfer calculations for finer scales depends on our understanding of 3D radiative transfer in the atmosphere and validation against observed variability. To gather more observations of variability in total and spectral solar irradiance at the cloud scale, we have developed low-cost radiometers to be deployed in spatial network setups (Heusinkveld et al., 2023). The design philosophy is similar to that of the Autonomous cold POoL LOGger (APOLLO) network (Kirsch et al., 2022): autonomously running low-cost instruments optimised to capture fluctuations accurately rather than high-accuracy single-point data. With calibration against expensive, high-quality reference stations, these instruments give useful information at a fraction of the cost while also being flexible in their setup, necessary to cover densely and maintain a large area.

In this article, we describe the deployment and measurement analyses of a network of 20–25 radiometers in two field campaigns in 2021, namely Field Experiment on submesoscale spatio-temporal variability in Lindenberg (FESSTVaL) and Land surface Interactions with the Atmosphere over the Iberian Semi-arid Environment (LIAISE). Both campaigns were organised to observe and understand local meteorology: FESSTVaL is focused on submesoscale variability and cold pools from convective storms and LIAISE is aimed at observing the land–atmosphere coupling from irrigated crop fields to the regional scale in complex terrain. The detailed observations of the atmosphere gathered by other groups during these campaigns are essential for understanding what we see in our own measurements. Section 2 covers the design and limitations of the radiometers, our network measurement strategy at both campaigns, including a brief description of the

weather, and a technique we use to construct spatial patterns from spatiotemporal data. What follows are three sections of results, each with their own calibration and validation discussion. First, we discuss three spatial patterns of broadband irradiance (Section 3), followed by a study of how the visible part of the spectrum changes in these cases (Section 4), and thirdly how irradiance varies in clear-sky conditions linked to water-vapour variability (Section 5). Conclusions and impacts of our results for solar-irradiance variability research are discussed in Section 6.

2 | METHODOLOGY AND CAMPAIGNS

2.1 | Solar irradiance sensor design

The sensors we use have been designed specifically to capture the fastest cloud-driven fluctuations of incoming sunlight and variations in the light spectrum induced by the atmospheric composition, clouds, aerosols, and vegetation. At a sampling frequency of 10 Hz, the Fast Response Optical Spectroscopy Time synchronised instrument (FROST: Heusinkveld et al., 2023) measures incoming shortwave irradiance at 18 wavelengths in the visible to near-infrared spectrum (410–940 nm). The locations of the 18 bands are detailed in Figure 1, which shows the response curves for the factory specification of 20 nm full-width at half maximum, combined with a simulated solar spectrum of a midlatitude summer day around solar noon. The 18 bands are spread over three subgroups of six bands on the spectrometer chip, which are colour-coded in the figure. Since these three subsensors are separated spatially by about a centimetre (in a triad), we use a Teflon diffuser on top to distribute incoming sunlight equally.

Material costs for one sensor are under 200 euros in total, they are powered by their own small solar panel, and are all time-synchronised using a global positioning system (GPS) chip. This makes them scalable and easy to deploy on tripods in field campaigns in flexible setups compared with conventional high-quality (10 times or more expensive) pyranometers or spectrometers. The low-cost design philosophy is a trade-off against accuracy compared with high-end instrumentation, but performance is good enough to capture and analyse spatial surface irradiance patterns driven by clouds and spectral signals of these variations. We focus on the practical application of the sensor in this work, but a complete and technical reference with more use cases is described in Heusinkveld et al. (2023). Important sources of error are discussed next, which we either correct for or take into account in the analysis presented in Sections 3–5.

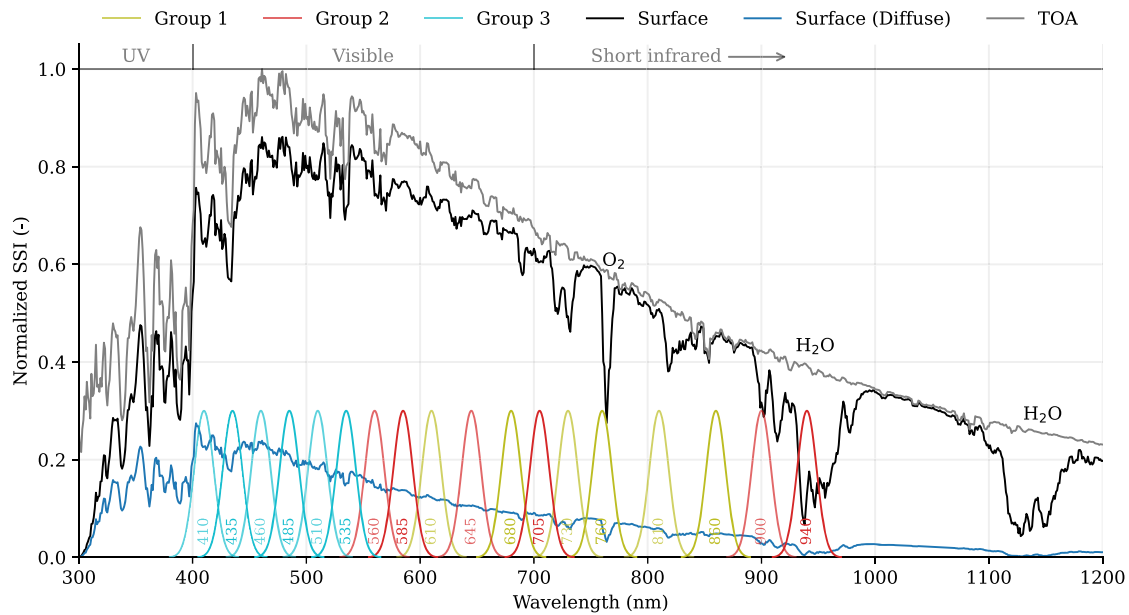


FIGURE 1 Spectral solar irradiance and the radiometer wavelength bands. Each radiometer band is colour-coded according to the sensor subgroup. Normalized top-of-atmosphere and surface solar spectral irradiance are based on a clear-sky simulation using libRadtran (Emde et al., 2016) for June 18, 2021, 1130 UTC, FESSTVaL campaign area in Germany (Section 2.5). Spectra are smoothed with a 5-nm rolling mean for readability. [Colour figure can be viewed at wileyonlinelibrary.com]

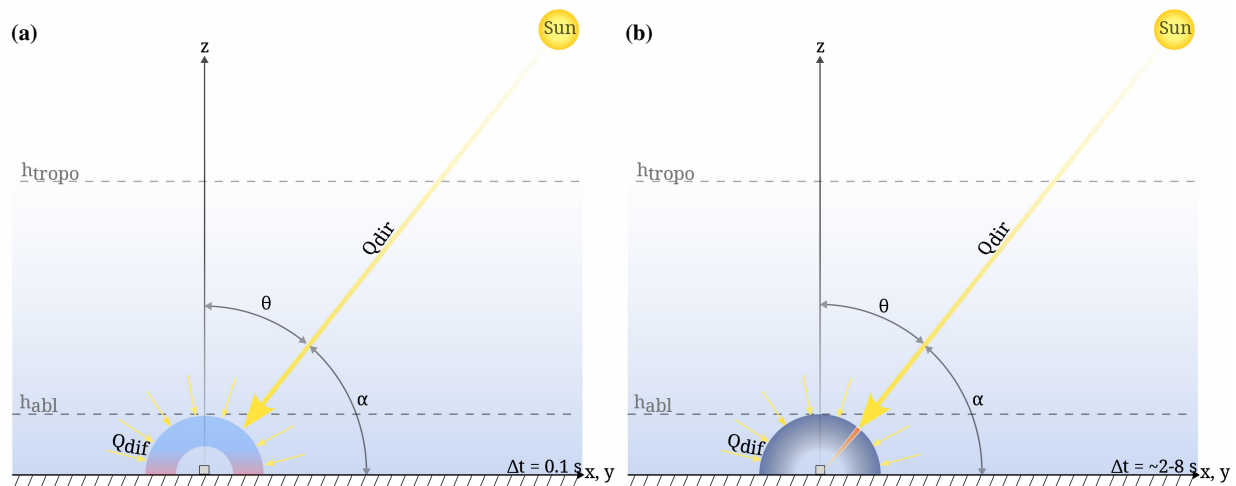


FIGURE 2 Schematic of surface solar irradiance measurements using (a) FROST and (b) a suntracker with a pyranometer and pyrhelimeter, both located at the grey square on the axis origin. The solar elevation angle α depicts the origin of direct irradiance Q_{dir} , of which a fraction (typically 10%–30%, see Figure S1) scatters and results in diffuse irradiance Q_{dif} , in this clear-sky example. FROST does not distinguish between Q_{dir} and Q_{dif} , and misses part of the signal originating from low angles α , illustrated by the red part of the semicircle in (a). A suntracker measures Q_{dir} and Q_{dif} separately, illustrated by the 5° arc and semicircle in (b), and is less biased for small α . The blue background gradient illustrates decreasing air density with height, while h_{tropo} and h_{abl} are the approximate tropopause and atmospheric boundary-layer heights. Δt denotes the resolved temporal resolution of each instrument. [Colour figure can be viewed at wileyonlinelibrary.com]

2.2 | Sources of measurement error

2.2.1 | Cosine response

Given a solar zenith angle θ , the horizontally measured signal strength of a constant light source Q as function of

θ would ideally be $Q \cdot \cos(\theta)$, see also Figure 2. In practice, there is an increasing relative underestimation of irradiance for high θ in our instrument (Figure 2a), referred to as the cosine response, for which we correct in postprocessing. While this cosine response correction is in principle a function of $\cos(\theta)$ as well, the triad sensor design results

in a unique response curve for each subsensor, despite the diffuser, which is also a function of the orientation of the sensor with respect to the Sun. This means that it is important to keep the sensor orientation constant throughout a measurement campaign, and ideally all sensors in a network are placed in the same orientation to minimise variations among sensors. The variation in cosine response between subgroups is relevant for the usability of the ratio between spectral bands, which we make use of in Sections 4 and 5, as these bands can be in different subgroups. This generally limits the use of spectral analyses to zenith angles of about 65° or below. Relative errors in spectrally integrated irradiance will also become pronounced at zenith angles of 75° or higher.

2.2.2 | Build and placement consistency

All instruments are hand-made, which leads to small imperfections or inconsistencies, such as the exact distance and position of the spectrometer from the diffuser. It is also challenging to place and keep all sensors level within a tolerance of 0.5° from day to day. This results in measurable variations among instruments, more noticeable at high zenith angles, and imposes a limit on what is achievable through postprocessing. While ideally there would be one universal calibration for all instruments, we find the best overall results when calibration is fine-tuned per individual instrument when possible. This ultimately leads to a limitation in accuracy, which we quantify as the spread among sensors in a network.

2.2.3 | Crosstalk

The third group of wavelength bands in particular (Figure 1) experiences significant crosstalk, meaning a sensitivity to wavelengths λ_{ct} outside the specified range of the band. Under worst-case conditions (a flat spectrum of light plus a 10.6-mm Teflon diffuser) the 410, 435, and 460 nm bands derive $\sim 70\%$ of their total signal from $\lambda > 750$ nm. In reality, the solar spectrum is significantly less energetic for λ_{ct} compared with 410–465 nm, effectively halving the crosstalk. The bands of group 1 in Figure 1 are all affected less than 10%, while effects for the second group are between 10% and 20%, except for 585 nm with $\sim 35\%$ crosstalk. This issue is resolved in a new version of the instrument by using certain wavelength filters over the affected subsensors (Heusinkveld et al., 2023), but the sensor version used in this work is still without such filters. Since the crosstalk effectively adds extra signal to be used when integrating spectra to broadband irradiance, we use all 18 bands in Section 3. For spectral analyses, we quantify

the effect crosstalk has on measured changes in irradiance spectra and choose bands that are least affected. Response curves for each band and diffuser are shown, and available as supplementary material, in Heusinkveld et al. (2023).

2.2.4 | Temperature sensitivity

There are two components introducing a temperature sensitivity in the instrument, with no significant difference across wavelengths. A small, linear change in signal strength of -0.25% per $+10$ K comes from the spectrometer itself. The Teflon diffuser has a $+2\%$ jump in transmittance from 20°C to 21°C , and declines slowly at a rate of approximately -0.4% per $+10$ K afterwards. While 10-cm or 2-m air temperature is known for all measurements, it does not translate directly to Teflon diffuser and spectrometer temperature, making a temperature correction nontrivial. We use measured surface temperature T_s (10 cm) as a proxy for qualitative assessment of measurement quality, while keeping in mind that T_s is still an underestimation. The role of temperature in measurement accuracy is discussed further in Section 3.1 on broadband calibration.

2.2.5 | Factory calibration

Because of limitations of the spectral quality in the sensor version used in this research, it is not easy to derive accurate measurements in $\text{W}\cdot\text{m}^{-2}\cdot\text{nm}^{-1}$. However, ratios between certain bands and changes therein contain valuable information and can be found in native sensor units, that is, without calibration. Sensor-to-sensor and wavelength band-to-band variation in factory calibration accuracy is generally $\pm 10\%$, with some outliers up to $\pm 20\%$, which also affects ratios between bands among sensors (Figure S2a). Even though each sensor can be treated separately in some cases, it often helps to have homogeneous raw output among sensors for a given light signal. We therefore homogenise the factory calibration as well as possible using a clear-sky periods where all sensors should measure the same, prior to performing any spectral analyses. This reduces the spread to within 2% (Figure S2b) and produces a dataset labelled as “precalibration”, which is the starting point for spectral analyses presented in this study.

2.2.6 | Maintenance and quality control

We performed irregular but frequent maintenance on the sensors during the field campaigns, usually early or late in the day, to check whether they were still running, level,

and free of dirt or dust (birds or flies liked to sit on some particular sensors). All data are provided with quality flags that mark data points with bad or unreliable data, due mostly to periods of sensor maintenance. In addition, temporary displacement of sensors or the obscuring of direct sunlight by nearby objects at low solar angles (trees, crops, other instrumentation) is flagged.

2.3 | Measurement strategy in field campaigns

We participated in two major field campaigns aimed at observing local- to regional scale atmospheric dynamics and land-atmosphere coupling: two weeks in June 2021 during FESSTVaL Hohenegger et al. (2023) in northeast Germany, and two weeks in July 2021 during LIAISE¹ in northeast Spain. Differences between the two campaigns in climate, local atmospheric dynamics, time of year, and geographical location have offered a diverse range of solar irradiance conditions to observe through the network of sensors, resulting in a total of ~4 weeks of spatial measurements. The campaigns and sensor network measurement strategy are described next.

2.3.1 | FESSTVaL

During the FESSTVaL campaign, we deployed a network of 20 sensors in a simple, equidistant rectangular grid.

Our measurements took place between June 14 and June 29, 2021, at the Falkenberg supersite of the Deutscher Wetterdienst, ~50 m above sea level. Figure 3a shows the 4 by 5 sensor network layout with a 50-m horizontal grid spacing. The choice of grid spacing is a combination of aiming for something that resembles the grid of a high-resolution cloud-resolving model, an a priori estimate of the required resolution to resolve shadow/sunlight transitions, practical constraints of the Falkenberg site, and the number of sensors we had available. Technically, the grid spacing was 49 m due to the constraints of rolling out the sensor network so that it is obstructed as little as possible by, or is not in the way of, other instrumentation on the field.

We deployed two consumer action cameras (with an on-board GPS clock) at the northern two grid corners to take time-lapse photos of the sky at 5-s intervals, so that we can relate the cloud field to surface irradiance. These cameras were oriented up towards the Sun in the southeast for the northwestern camera, and southwest for the northeastern camera. Calibration of the sensors is done against the Falkenberg suntracker, equipped with high-quality instrumentation and located in the southeast corner of the field. Instrument locations relative to the grid are illustrated in Figure 3a.

In addition to this setup, three sensors (1, 22, 23) were located several kilometres to the west, south, and east of the field (Figure 3b), to capture part of the larger scale variability in the campaign area. Two other supersites are

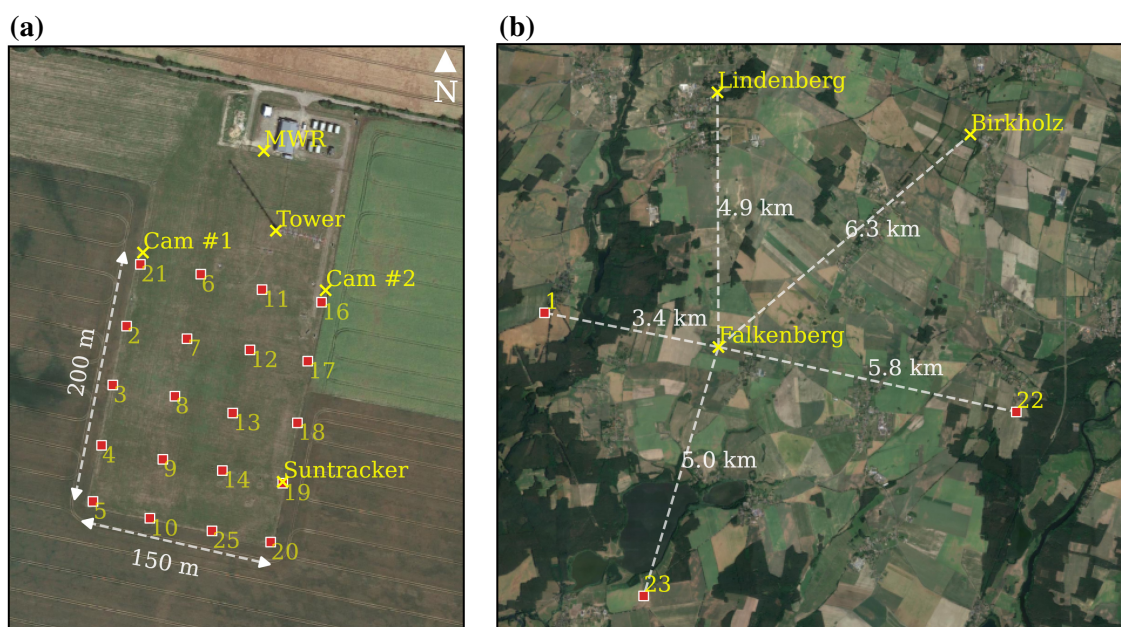


FIGURE 3 Radiometer network measurement layout at FESSTVaL. (a) The 4 by 5 sensor grid at Falkenberg with a horizontal spacing of ~50 m, together with the 98-m tower, suntracker, two cloud cameras, and microwave radiometer (MWR) locations. Number labels are sensor IDs. (b) Additional sensors set up in the FESSTVaL campaign area around Falkenberg, including the location of the FESSTVaL supersites Lindenberg and Birkholz. Background satellite data: Google Maps © 2024. [Colour figure can be viewed at [wileyonlinelibrary.com](https://onlinelibrary.wiley.com/doi/10.1002/qj.4712)]

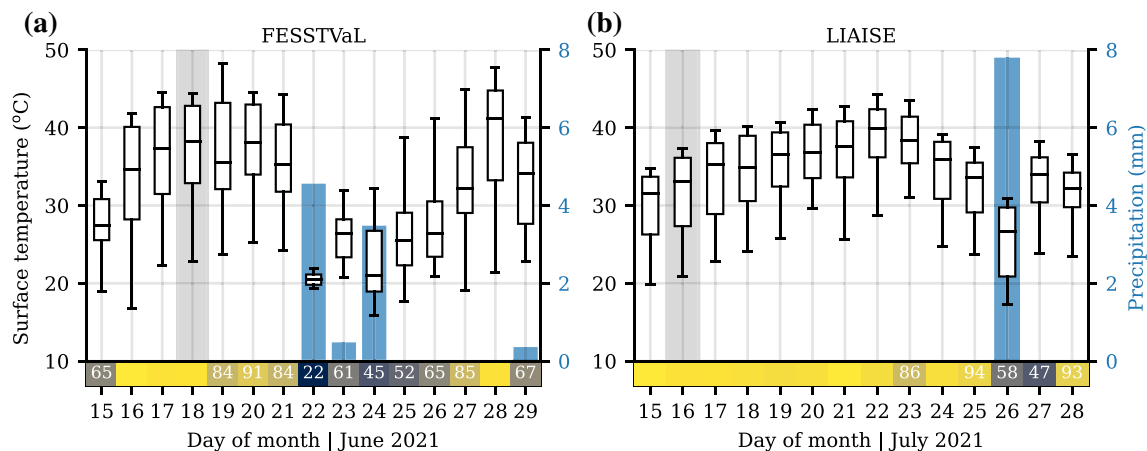


FIGURE 4 Overview of weather variables most relevant for irradiance measurements at FESSTVaL and LIAISE. All data are during daytime (solar elevation angle $>15^\circ$). Box plots are the surface temperatures at (a) Falkenberg and (b) Els Plans. The blue bars are accumulated precipitation during daytime at the sensor network. The colour shading at the bottom is the observed percentage of clear-sky irradiance (CAMS McClear), where darker colours indicate more cloudiness, labelled with numbers for values $< 95\%$. Vertical grey bars on June 18 and July 16 are the reference cloud-free calibration dates used in Section 3. [Colour figure can be viewed at [wileyonlinelibrary.com](https://onlinelibrary.wiley.com)]

Lindenberg and Birkholz, and all supersites were equipped with microwave radiometers which measure integrated water vapour, used in this study, among other things. There were many more instruments deployed.² Our two weeks at FESSTVaL featured one fully clear-sky day and one rainy day with thick cloud cover, but was otherwise characterised by many different (broken) cloud covers (Figure 4a).

2.3.2 | LIAISE

Between July 14 and 30, 2021, we set up a network of sensors at the La Cendrosa site of the LIAISE campaign.³ La Cendrosa is located within an irrigated part of an otherwise semi-arid region, with complex local, regional, and mesoscale dynamics (Mangan et al., 2023). The typical expected and observed (see Figure 4b) summertime weather in this region in northeastern Spain is cloud-free, dry, and hot. Specifically at La Cendrosa, due to local topography and sea-breeze dynamics (locally called “Marinada”), prevailing daytime winds are westerly, shifting via a southern sea breeze to easterly night time winds. While the goal is primarily to observe cloud-driven irradiance variability, frequent clear-sky days offer a good calibration opportunity and allow analyses in spectral variations due to day-to-day variations in aerosol and water-vapour content. We had a bit more space to set up the network compared with Falkenberg, so, in an attempt to capture larger patterns, we decided on a grid spacing of 100 m. With the prevailing westerly daytime winds, we oriented the grid in a similar direction, in hopes of tracking cloud shadows and enhancements over a length of 400 m, illustrated in

Figure 5a. An additional group of radiometers was set up in the footprint of the scintillometer, which in the context of this study gives additional resolution in the grid centre, but makes the total network nonequidistant.

Two action cameras were mounted on the energy balance station (EBS), west and east oriented, but pointed straight ahead rather than at the Sun to include a visual record of the vegetation growth and irrigation during the campaign period. The EBS measures incoming broadband irradiance as part of the radiation-balance measurements, used in this study as a calibration reference. Hourly boundary-layer soundings were deployed at La Cendrosa during Intensive Observation Periods (IOPs), which we combine with hourly full troposphere soundings at the nonirrigated site Els Plans (Figure 5b), located 14.1 km to the southeast. There are many more observations and sites within the campaign area, which can be found at <https://liaise.aeris-data.fr/>.

2.4 | Visualising spatial patterns

We find, as will be shown shortly, that cloud shadow and enhancement patterns often both exceed the network size and have details finer than the network resolution. It is furthermore challenging to visualise a high amount of spatiotemporal data in a concise way without applying statistics. For some figures, we therefore apply a data-processing technique that makes use of the high temporal resolution and an estimate of the cloud velocity in order to increase the effective network size and spatial resolution. Essentially, the following technique transforms temporal data to spatial data. The technique assumes

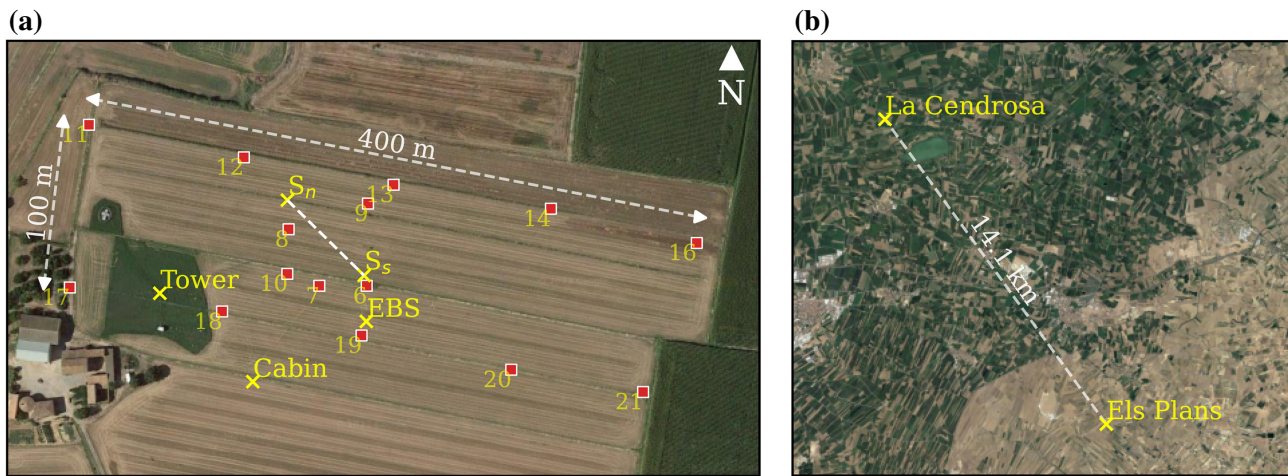


FIGURE 5 Sensor network measurement layout at LIAISE. (a) The west–east oriented 5 by 2 sensor grid at La Cendrosa has a horizontal spacing of ~ 100 m, with an additional set of five sensors within the footprint of the scintillometer (S_n to S_s). The reference pyranometer is mounted on the energy balance station (EBS). (b) La Cendrosa and Els Plans, illustrating the irrigated (green) versus nonirrigated (beige) area. Background satellite data: Google Maps © 2024. [Colour figure can be viewed at [wileyonlinelibrary.com](https://onlinelibrary.wiley.com)]

clouds retain their shape (analogous to Taylor’s hypothesis of frozen turbulence) when moving over the measurement network (a schematic example is available in Figure S3). For example, we can “advect” the Falkenberg network (Figure 3a) in space with a time step of 5 s and $5 \text{ m}\cdot\text{s}^{-1}$ cloud velocity for 10 steps, effectively resulting in a spatial network of 200 points ($20 \text{ sensors} \times 10 \text{ steps}$) that spans $\sim 450 \text{ m}$ ($5 \text{ s} \times 5 \text{ m}\cdot\text{s}^{-1} \times 10 \text{ steps} + \text{original network length of } 200 \text{ m}$) in the advection direction and has approximately double the resolution (one step is 25 m). The virtual 200 points can then be interpolated to a new equidistant grid for easier comparison and visualisation.

The main challenge with this technique is the determination of the cloud-velocity vector, which we initially base on wind speed at cloud level from nearby soundings and ceilometer data and then fine-tune manually to produce a result as smooth as possible. Small changes in direction or speed quickly result in noisy results, with artefacts from incorrectly placed data points reporting contradicting values. Keeping the total integration time short minimises our violation of the static cloud shapes assumption, though some artefacts can remain. The cloud-velocity step fine-tuning needs to be repeated frequently, every 10–30 min or so, due to wind and cloud velocity (subtly) changing or simply varying among clouds. Results are consistent when this exercise is repeated with selective omission of sensors, with mean absolute errors and root-mean-square errors between 0 and 5% of the total variation in irradiance (see Figures S4 and S5 for examples). We apply this technique to three distinct cases, first shown in Section 3.

2.5 | Simulated solar position, clear-sky irradiance, and irradiance spectra

In addition to observations, we require extra information about solar irradiance, mostly for the interpretation of measurements. An estimate of clear-sky irradiance is required for identifying cloud-enhancement events in the measurements, which we base on the globally available Copernicus Atmospheric Monitoring Service (CAMS) McClear product (Gschwind et al., 2019). This product is based on a radiative transfer model that calculates, for a cloud-free atmosphere, global horizontal (and diffuse) irradiance, given a geographical location, time of year, and time of day. Included in these calculations is the atmospheric composition based on three-hourly CAMS analyses (aerosols, water vapour, and various other gases). Accuracy of global horizontal irradiance is within several per cent (Gschwind et al., 2019), enough for our purposes in this study, as we will look at measurements of significantly larger variations. It is available at a 1-min resolution, which we interpolate linearly to 1 s when necessary.

For both context and independent validation of measured spectral irradiance, we calculate clear-sky shortwave irradiance spectra using libRadtran (Emde et al., 2016). Aerosols are set to default (rural-type boundary-layer aerosol), total column water vapour is taken from microwave radiometer (FESSTVal) or sounding (LIAISE) measurements, surface albedo is set to “cropland”, and other atmospheric profiles are set to the “midlatitude summer” default. Other relevant settings are the coordinates and time of day, which are case-specific. Validation

of the setup is done using four clear-sky moments of the FESSTVaL campaign: 0800 UTC on June 17, 18, 27, and 1130 UTC on June 18. Values of clear-sky irradiance overestimate the Falkenberg suntracker observations by 0.8%–1.0% ($5.5\text{--}7\text{ W}\cdot\text{m}^{-2}$) for the 0800 UTC cases, and by 1.3% ($11\text{ W}\cdot\text{m}^{-2}$) for 1130 UTC on June 18. Performance for diffuse irradiance is significantly worse, likely due to using prescribed default aerosols, and is overestimated in all cases between 25% and 34%, except for 0800 UTC on June 17 with 9%. The impact of this bias is small in the context of this study, but will be taken into account when results are discussed. An overview of all simulations with validation statistics is available in Table S1. The spectrum of June 18 at 1130 UTC is illustrated in Figure 1.

Finally, for sensor cosine response corrections and calibration, we need accurate solar zenith and azimuth angles, which we calculate using PySolar (Pingswept, 2022).

3 | SPATIAL PATTERNS OF SURFACE SOLAR IRRADIANCE

3.1 | Deriving global horizontal irradiance

Broadband solar irradiance is the total shortwave surface solar irradiance, often called global horizontal irradiance (GHI). GHI is measured using pyranometers, or in combination with pyrhemimeters (Figure 2b), and typically has a spectral range encompassing most or all of the shortwave

irradiance spectrum (e.g., 200–3600 nm for the CMP22: Kipp and Zonen (2004)). This range exceeds the spectral range covered by the 18 wavelength bands of our sensor (410–940 nm, a bit more including the crosstalk sensitivity), but these bands cover the most energetic part of the spectrum (410–940 nm $\approx 68\%$ of total irradiance based on data in Figure 1). We derive the GHI by first taking the mean of all spectral bands (Figure 1), correcting for the cosine response, and converting raw measurement units, $\text{count}\cdot\text{bin}^{-1}\cdot\Delta t^{-1}$, to $\text{W}\cdot\text{m}^{-2}$. This calibration generalises under the assumption that the spectrum shape of short-wave irradiance remains constant.

For both FESSTVaL and LIAISE, we have at least one clear-sky day with high-quality reference GHI measurements available from pyranometers to calibrate against. The cosine response is a function of solar zenith angle, so we take the ratio between the spectral average of our instrument and the reference GHI measurement as a function of this angle. Figure 6a shows the resulting ratio curve relative to the suntracker reference for a single radiometer at FESSTVaL for a clear-sky day (June 18, 2021). The best curve fit was extrapolated from 15 to 10° and kept constant for any value below, because here the absolute signal becomes too low and relative measurement errors, including that of the pyranometer cosine response, negatively impact the curve fit. In particular, differences between the cosine response of each subgroup become more pronounced at such low angles. Furthermore, when the sensor is not perfectly level, measured incoming irradiance between morning and evening for the same solar elevation

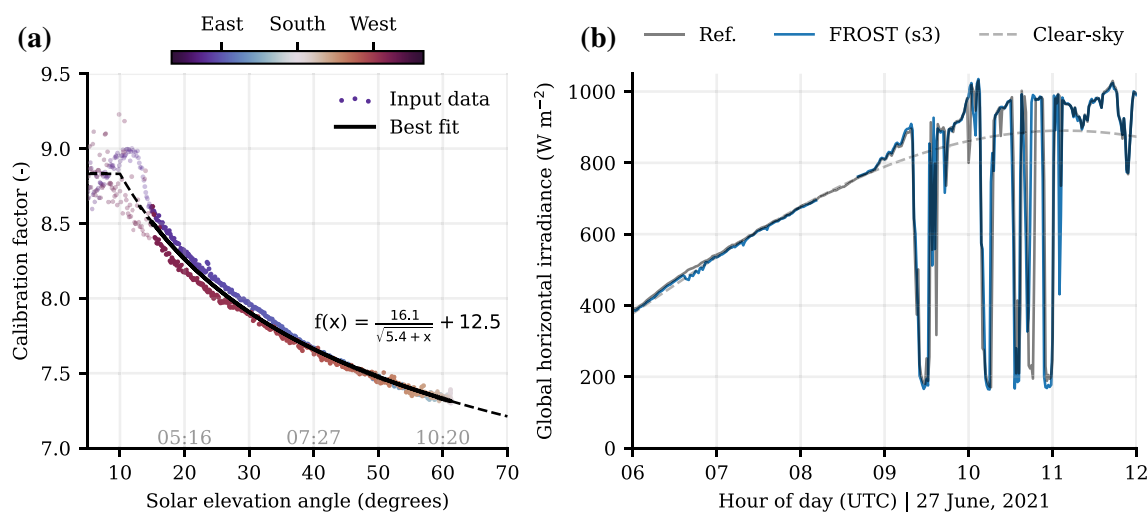


FIGURE 6 Broadband global horizontal irradiance calibration example. (a) Calibration factor as a function of solar elevation angle between raw instrument data and the irradiance data from the Falkenberg suntracker for June 18. The best-fitting curve is manually extended at the lower and upper end of the data range (dashed line) and follows the function with best-fitting coefficients between 15° and 60° elevation angle. Time at the bottom is in UTC for morning until noon. The scatter colours indicate the solar azimuth angle. In (b), the best-fitting calibration from (a) is applied to measurements of June 27, and compared again with the Falkenberg suntracker reference. All FROST data shown are for sensor 3, resampled to 1 min. [Colour figure can be viewed at [wileyonlinelibrary.com](https://onlinelibrary.wiley.com/doi/10.1002/qj.4712)]

angle introduces an asymmetry, which explains part of the hysteresis effect visible in Figure 6a. We find that a fitting technique that takes the solar azimuth angle into account and fits on subgroups separately does not generalise beyond the calibration data, and thus does not improve data accuracy for days with clouds. This is likely due to slight variations (less than 0.5°) in sensor orientation that may occur from day to day, the exact reasons for which we do not know, and different combinations of solar elevation and azimuth angle as the Earth's orbit around the Sun progresses. Figure 6b illustrates the resulting time series when the reference date best fit is applied to a different day (June 27, 2021). This examples shows that sensor 3 captures both the daily cycle and cloud-driven fluctuations.

We apply this calibration routine to all data for each sensor individually, for both campaigns separately. Figure 7 gives an overview of the performance of all grid sensors across all campaign days for FESSTVaL and LIAISE, compared with their respective reference station. Overall, the bias is within 2%, and mean absolute error (MAE) between 5 and $15 \text{ W}\cdot\text{m}^{-2}$ for most days and sensors. Notable outliers, June 22 or July 26 and 27, are explained by overcast and rainy weather (Figure 4), which leads to increased absorption in mostly near-infrared wavelength bands that our instrument does not sample, is part

of the shortwave spectrum. GHI is thus overestimated, because clear-sky conditions with less relative absorption in the near-infrared are the basis for calibration, violating our assumption that the solar spectrum shape is constant under all conditions (see section 3.3 of Heusinkveld et al. (2023) for more details). Sensor-to-sensor variations are typically smaller than or equal to the error with respect to the reference station, and likely originate from variations in construction and minor day-to-day changes in sensor orientation. Changes in calibration quality due to the sensors' temperature sensitivity are small, as for most days the measured 10-cm temperature, and therefore the Teflon diffuser temperature, was well above the 2% signal jump at 20°C (Figure 4).

3.2 | First impression and video

To get a first impression of cloud-driven patterns of surface solar irradiance, we plot the sensor network directly on a map combined with the cloud camera images, and render frames for each time step to create a video. For June 27, 2021, a day with cumulus clouds at FESSTVaL, such a video is available in the Supporting Information or at <https://vimeo.com/827602111>. One frame is displayed

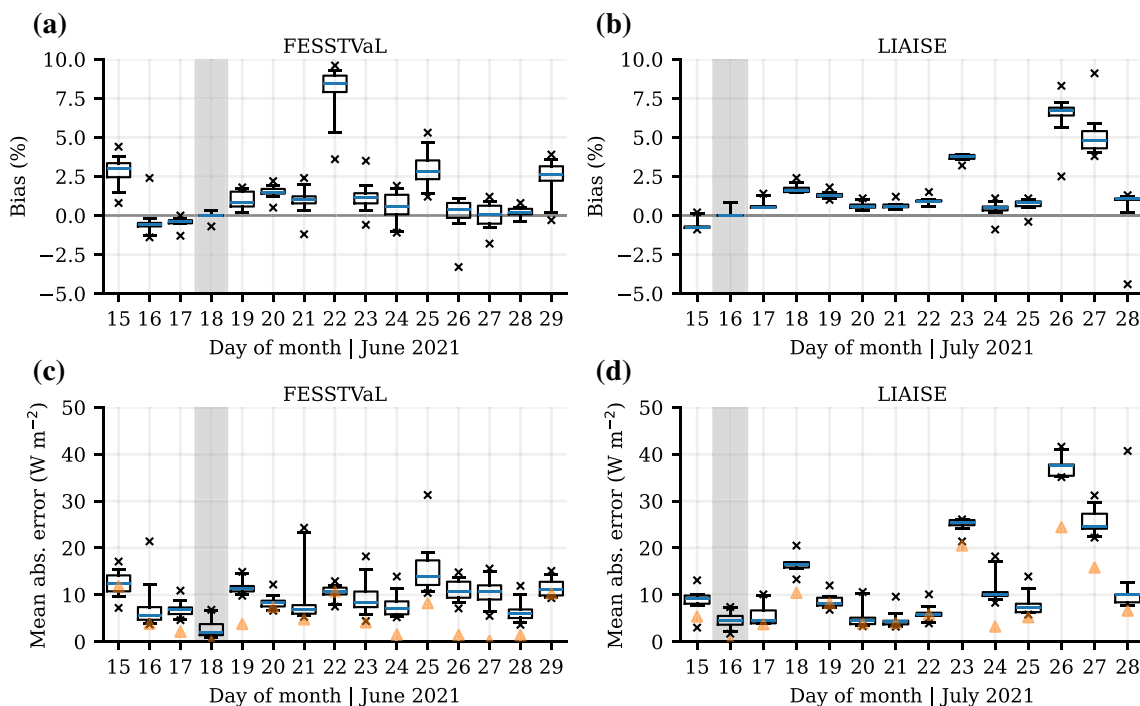


FIGURE 7 Global horizontal irradiance calibration performance of all sensors for FESSTVaL and LIAISE. (a,b) Mean bias of daily sums of irradiance compared with a reference pyranometer for all sensors, and (c,d) the mean absolute error. Vertical shading indicates the reference clear-sky calibration date for FESSTVaL in (a,c) and LIAISE in (b,d). Box plots span the 5th–95th percentile range of the spread among sensors. The orange triangle markers in (b,d) indicate the absolute median bias in $\text{W}\cdot\text{m}^{-2}$. Only data with solar elevation angle above 15° are used for verification. [Colour figure can be viewed at [wileyonlinelibrary.com](https://onlinelibrary.wiley.com)]

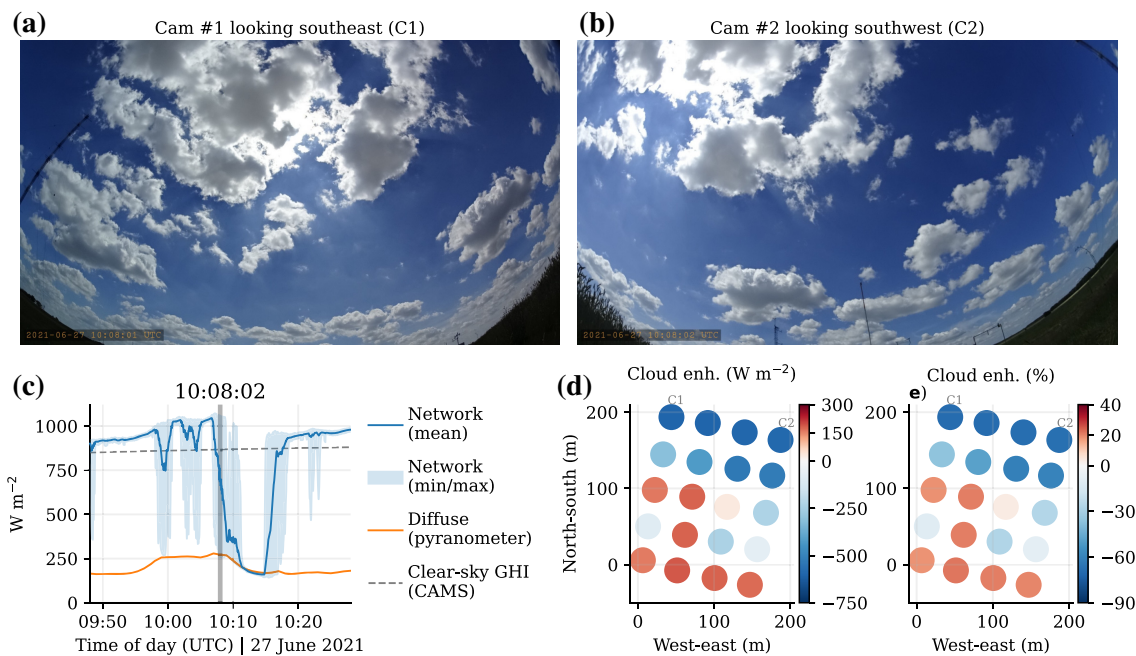


FIGURE 8 Network measurements of GHI combined with cloud imagery for June 27, 2021, at Falkenberg (FESSTVaL campaign). The cloud images in (a) and (b) come from two action cameras located in the northern corners of the network. The time series (c) are centred around the 1100 UTC snapshot and feature diffuse irradiance from the Falkenberg suntracker, clear-sky GHI, and the FROST network measurements (spatial mean and min/max range). The network measurements are plotted relative to clear-sky GHI (CAMS McClear) in (d) absolute and (e) relative units. For an animated version, see the supplementary material or <https://vimeo.com/827602111>. [Colour figure can be viewed at wileyonlinelibrary.com]

here in Figure 8, but in particular the video shows how the sensor network captures irradiance patterns made by the dynamic cumulus field. An interesting feature is how some cloud passages show a clear temporary increase in diffuse irradiance, whereas for others the diffuse irradiance remains constant, but always higher than clear-sky irradiance. The example shown in Figure 8 shows a fractured cloud passage (a,b) with a local increase in diffuse irradiance leading to relatively stronger enhancements or irradiance (c–e) compared with other cloud passages. There is an extra step of complexity once cirrus fields pass over, superimposing their effect onto that of the boundary-layer cumuli. It is also clear that the spatial scale of cumulus shadows and enhancements is well above that of the network size and transitions between shaded and sunlit areas occur at scales smaller than the network sensor spacing.

As an illustration of overall observed variability throughout both field campaigns, we construct a power density spectrum of all time series in FESSTVaL, LIAISE, and for three cases separately, illustrated in Figure 9. The campaign averaged spectra follow approximately $f^{-5/3}$ scaling between 10^{-4} and 10^{-1} s^{-1} , before a scale break between 10^{-1} and 10^0 and an apparent continuation of weaker power-law scaling thereafter. Similar $f^{-5/3}$

scaling is shown by Tabar et al. (2014) until $\sim 10^{-1} \text{ s}^{-1}$, after which it deviates similarly. The scale break between 10^{-1} and 10^0 s^{-1} is expected, at least for broken cloud conditions, due to the smallest clouds becoming transparent to solar irradiance (Mol, van Stratum, et al., 2023), making the biggest source of variability disappear. Other studies using spatial pyranometer networks find clearly different spatiotemporal scales and magnitude of variability for different sky types, and identify “broken clouds” as the most potent for generating variability at the smallest scales (Lohmann et al., 2016; Madhavan et al., 2017). Power density spectra for single sensor time series of clear-sky (June 18), overcast (June 22), and cumulus (June 27) show differences in power-law scaling in the 10–3600 s range, the variance in cumulus dominating over other sky types across all scales, and overcast conditions having the lowest variance of all sky types at scales shorter than 10 s, all consistent with spatial wavelet variance presented in Madhavan et al. (2017) (their fig. 5). Grid-averaged spectra start to deviate from single-point measurements at scales shorter than 10 min. The spectral power of the Falkenberg grid average is an order of magnitude below that of a single sensor at these small scales, relatively consistent between the three sky types.

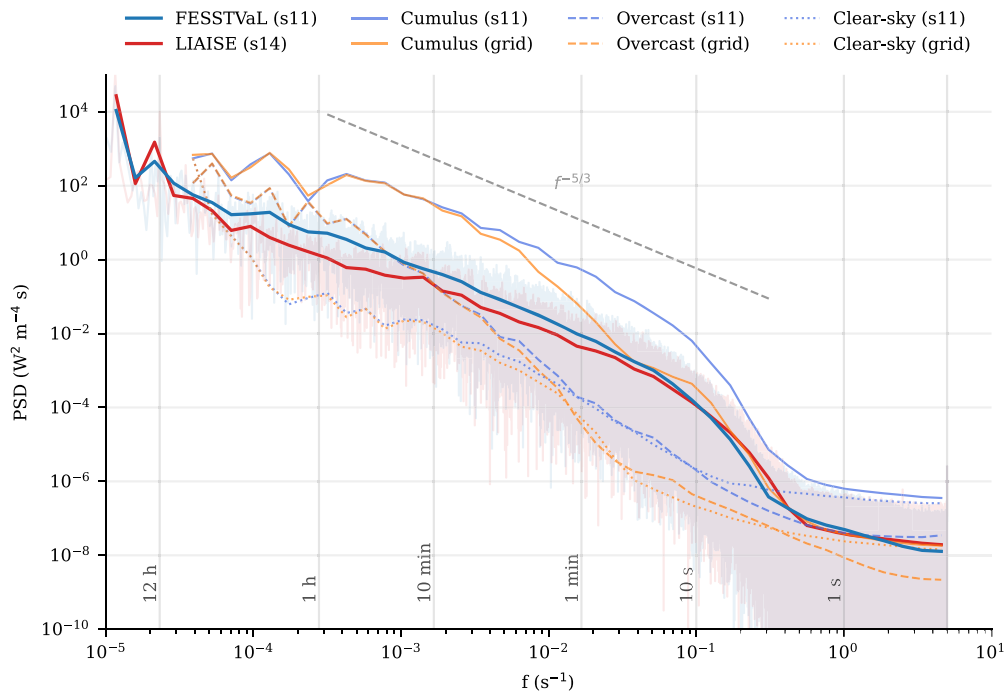


FIGURE 9 Power density spectra for global horizontal irradiance time series of the whole FESSTVaL and LIAISE campaigns. Cumulus (June 27), overcast (June 22), and clear-sky days (June 18) are illustrated separately for both a single sensor and the average of the Falkenberg grid. [Colour figure can be viewed at [wileyonlinelibrary.com](https://onlinelibrary.wiley.com)]

3.3 | Three types of patterns

Often, during the campaign, a combination of cloud types are present with varying degrees of total cloud cover and optical thickness: for example, a mix of cumulus (passive to deep convective), multiple layers of altocumulus, and/or cirrus. To demonstrate the diversity of observed surface irradiance variability during the campaigns, we select three cases. These selected cases are of cloud types that occur in isolation, making the interpretation easier, and are frequently present in the campaign period: (1) boundary-level cumulus, (2) mid-level altocumulus, and (3) high-level cirrus, illustrated in Figure 10. The patterns are visualised using the technique explained in Section 2.4, and are robust to sensor exclusion tests (shown in Figures S4 and S5 for the first two cases).

The first case (Figure 10a–c) is from the same date as Figure 8 (June 27, 2021), and features slow-moving ($4.5 \pm 1 \text{ m}\cdot\text{s}^{-1}$) fair-weather cumuli with cloud bases at $\sim 1750 \text{ m}$ and a relatively clean atmosphere (deep blue sky). Cloud enhancement to shadow transitions are very sharp, about 40–60 m as estimated from Figure 10b, making cumulus cloud shadows slightly smaller than their size with a length scale similar to what we found in Mol, van Stratum, et al. (2023) based on long-term time series. Diffuse irradiance does not vary significantly on the spatiotemporal scales of this example, suggesting the total light scattering off clouds in this case has a very wide horizontal range without much contribution to the total enhancement from local forward

scattering at transparent cloud edges. Around the smaller cloud fragments (1100–1105 UTC, bottom pattern in Figure 10b), we do observe an increase in cloud enhancement of $\sim 30\text{--}40 \text{ W}\cdot\text{m}^{-2}$ (4% of clear-sky), and overall the diffuse is lower after the passage (1110 UTC) than before (1050 UTC). We think the absence of diffuse peaks close to transitions in this case may be due to the relatively high cloud base, where forward scattering through cloud edges is spread out over a large surface area rather than more locally focused. However, the suntracker measurements are 1-min averages, so they may miss local peaks in diffuse irradiance, and changes in the sources of scattered light (overall cloud field vs. local cloud edge) could coincidentally be counteracting. The contrast between cloud enhancement and shadow is large, approximately $750 \text{ W}\cdot\text{m}^{-2}$, or 80% of clear-sky irradiance. Some of the artefacts arise from small biases between sensors, such as the horizontal stripes at 1050 and 1110 UTC, or likely changing cloud shape, such as the noisy pattern around 1106 UTC. Section 4 introduces a few more cumulus passages of this case, including spectral effects, to investigate further what is going on.

The second case (Figure 10d–f) is of an altocumulus field at 5 km altitude (estimated using the ceilometer of Falkenberg), moving at $14.3 \text{ m}\cdot\text{s}^{-1}$, and under overall hazier conditions than the first case. Individual altocumulus clouds are about 1–5 times the area of the sensor network based on the distance between cloud enhancement peaks, whereas these peaks are up to $\sim 200 \text{ m}$ in diameter and thus mostly fit within the network area. Apart from the spatial scales being significantly smaller than the

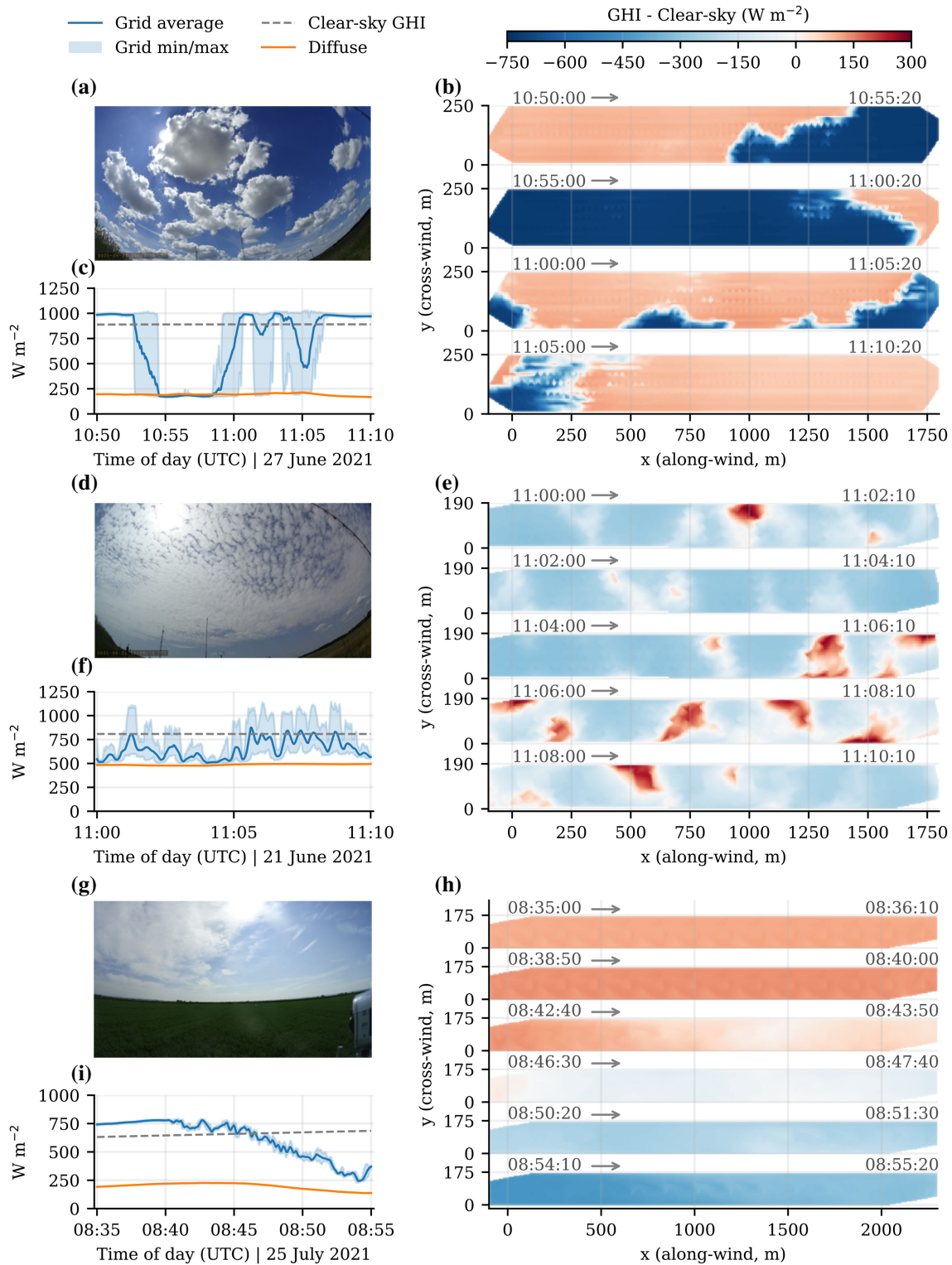


FIGURE 10 Spatial patterns of cloud enhancements and shadows for three cases: (a–c) cumulus, (d–f) altocumulus, and (g–i) cirrus. (a,d,g) show a representative photo. The time series include grid measurements (FROST network at $\Delta t = 1$ s), clear-sky GHI (CAMS McClear at $\Delta t = 60$ s), and diffuse irradiance ((c,f) Falkenberg suntracker at $\Delta t = 60$ s or (i) La Cendrosa energy balance station at $\Delta t = 5$ s). Data in (b,e,h) are plotted relative to clear-sky irradiance. The temporal range of each pattern segment is labelled in HH:MM:SS. [Colour figure can be viewed at wileyonlinelibrary.com]

cumulus case, the shadow patterns are weak ($250 \text{ W}\cdot\text{m}^{-2}$ or 35% below clear-sky), and cloud enhancements very strong, locally more than $300 \text{ W}\cdot\text{m}^{-2}$ or 40% above clear-sky. The mechanism appears to be a consistently high diffuse irradiance ($500 \text{ W}\cdot\text{m}^{-2}$, two-thirds of clear-sky) generated by forward scattering in the semitransparent altocumulus field as a whole, with superimposed gaps in the clouds that let up to $650 \text{ W}\cdot\text{m}^{-2}$ of direct irradiance pass through locally. These are thus particularly extreme variations at small spatiotemporal scales, with a similar relative magnitude (cloud shadow to enhancement contrast) to that of the previous example with cumulus clouds.

The third and last case (Figure 10g–i) is features an optically thick cirrus field moving over the LIAISE network setup at $35 \text{ m}\cdot\text{s}^{-1}$ (July 25, 2021) and is notably different from the other two cases. Only weak spatial patterns of about 500 m in length are visible in some parts of the cirrus (0843 and 0846 UTC for example, Figure 10h). Despite the high cloud velocity, it takes 15 min to go from $120 \text{ W}\cdot\text{m}^{-2}$ or 18% of cloud enhancement (0839 UTC) to a near-complete blocking of direct irradiance (0854 UTC). The area of influence of this patch of cirrus far exceeds the radiometer grid size, with the transition from cloud enhancement to shadow minimum covering $35 \text{ m}\cdot\text{s}^{-1} \times 900 \text{ s} = 31.5 \text{ km}$.

3.4 | Broadband patterns in summary

The scales of patterns caused by these three cloud types suggest that errors made by radiative transfer models using the independent column approximation (i.e., without 3D radiative effects) will be apparent in all cases. This is true not only for the smaller scales of broken boundary-layer clouds, but also for cirrus in coarser resolution medium-range numerical weather prediction (e.g., the European Centre for Medium-Range Weather Forecasts Integrated Forecasting System (IFS) at $\sim 9 \times 9 \text{ km}^2$). The characteristics of spatial surface irradiance patterns within the category of “broken cloud”, here extended beyond boundary-layer clouds, is large. Altocumulus clouds appear to be particularly effective in generating small-scale but large enhancements in surface irradiance (up to $\sim 200 \text{ m}$ in diameter, 40% above clear-sky). This effectiveness did not show up clearly in a multiyear analysis of cloud enhancements as function of cloud type (Mol, van Stratum, et al., 2023), possibly due to limitations of satellite resolution and pyranometer response time, but also Schade et al. (2007) identified altocumulus as very effective drivers of large peaks in surface solar irradiance. We therefore believe these (broken) mid- and high-level clouds are worth more attention, given that their global occurrence

is similar to that of cumulus (e.g., Sassen & Wang, 2008) and their (potential) effect on surface irradiance is large.

4 | SPECTRAL SIGNATURE OF CLOUD-DRIVEN IRRADIANCE PATTERNS

4.1 | Identifying changes in “blue” versus “red” light

Clear-sky conditions are famously characterised by blue skies (diffuse irradiance enriched in shorter wavelengths) and a yellow Sun (direct irradiance depleted of those same wavelengths), owing to the λ^{-4} dependence of Rayleigh scattering. An example of this spectral signature is illustrated in Figure 1. As clouds interact with both components of irradiance, we expect to see changes in the ratio between short and long wavelengths in our surface measurements. Such changes can help point to where the irradiance originates from and help us understand how a cloud field modifies surface irradiance. For example, if a single cumulus cloud in an otherwise clear sky blocks direct (blue-depleted) irradiance, we expect the spectrum of remaining light to have a larger share of short wavelengths relative to clear-sky conditions. In this section, we expand upon the three cases of Section 3 by analysing observed changes in the ratio of these short and long wavelengths, firstly to quantify spectral effects of clouds and secondly to help us understand these cases further.

Relating observed changes in short and long wavelengths to a different mix of clear-sky diffuse and direct sunlight means we assume no other factors influence the spectrum, and therefore requires scattering and absorbing of light by clouds to be constant with wavelength. This assumption holds for the visible (and most energetic) part of the solar spectrum (Ackerman & Stephens, 1987; Key et al., 2002; O’Hirok & Gautier, 1998; Schmidt et al., 2010), with all other conditions kept equal (aerosol amount, spectral surface albedo, gas concentrations). An exception may be the effects of hygroscopic growth of aerosols in air with high relative humidity, often found near cloud edges or recently dissipated clouds. Hygroscopic growth causes aerosols to scatter more despite constant aerosol amount, and more so for shorter wavelengths. This was found by Gristey et al. (2022), in cases of shallow cumuli, to be an important contribution to enhanced diffuse irradiance in cloud shadows from extra scattered light around the cloud. Given its wavelength dependence, it may in our analysis contribute to more “blue” cloud shadows. This contribution is not within our ability to quantify in

this study, but we take it into account when interpreting the results.

4.1.1 | Ratio calculation

In order to quantify changes in the wavelength ratio, we need to choose a set of bands in FROST and determine a reference value for clear-sky conditions. For the observed ratio, we combine multiple bands of the radiometer to get a stronger signal and limit our choice further by excluding bands of $\lambda < 485$ nm (too high crosstalk, Section 2.2.3) and $\lambda > 700$ nm (growing contribution of spectral effects of water). Specifically, we choose the bands $\lambda_s = (485, 510, 530$ nm) and $\lambda_l = (645, 680, 705$ nm) and define the ratio $r = \lambda_s/\lambda_l$ to represent “blue” versus “red” light. We define changes in r due to clouds as $\Delta r = r - r_{cs}$.

The clear-sky reference values r_{cs} , which depend on the solar zenith angle, can be derived in two ways. One involves extrapolating an observed r at a time before clouds form to a later time with cloudy conditions, based on how r changes in a cloud-free day. The drawback of this method is that it requires at least some part of the day to be cloud-free, which is often not the case, and assumes changes in r with solar zenith angle in a cloud-free day to generalise to other days. Alternatively, we therefore also simulate clear-sky spectra for each analysed case (see Section 2.5), which provides independent estimates of r_{cs} and helps validate the first approach. For the cases of June 17 and 27, we can use both methods (with June 18 as the clear-sky observed reference), which shows that observed and modelled r in clear-sky conditions at 0800 UTC are consistent. Furthermore, the modelled change in r between 0800 and 1130 UTC is nearly the same as in the observations of June 18 (+1.16% and +1.05%, respectively). For cases where we cannot use the first approach (June 21, July 25), we test the sensitivity of modelled r_{cs} for June 18 by, somewhat dramatically, doubling the total column water vapour or excluding aerosols. This results in a change of +1.5% and +1.2%, respectively, so we deem the sensitivity to either factor to be small and therefore the simulated r_{cs} to be accurate enough for our purposes. An overview of all simulations and ratios calculated from them is given in Table S1.

4.1.2 | Crosstalk correction

A caveat to estimating r using FROST is its crosstalk (Section 2.2.3). Under a flat spectrum, the crosstalks (ct) for the chosen bands are $ct_s \approx 45\%$, $ct_l \approx 14\%$ for λ_s , λ_l , respectively. Crosstalk is roughly halved for a more typical

clear-sky spectrum (as in Figure 1). We cannot correct for crosstalk a priori, because it would require knowing the spectrum of irradiance and how it changes, whereas this is what we want to measure and characterise. However, we can simulate how measured changes in r , Δr_m , relate to true changes Δr_t . Taking the clear-sky diffuse irradiance illustrated in Figure 1 and mixing in direct irradiance from 0 to 1.6 times the clear-sky value, we find a linear relationship $\Delta r_m = \gamma \Delta r_t$ and $\gamma \approx 0.5$, that is, measured changes are underestimated due to crosstalk (Figure S6). Both observations by Durand et al. (2021) (their fig. 2) and a simulation with a homogeneous water cloud (fval_j18_wc, Table S1) show that r would indeed decrease in overcast conditions compared with clear-sky, but that changes in the λ_{ct} range are insignificant. Furthermore, Heusinkveld et al. (2023) show that the sensor version without crosstalk has qualitatively the same effect of overcast compared with clear conditions (their fig. 17). We are therefore confident that the sign of change we observe is correct and that the magnitude of change is underestimated. Quantitative results will nonetheless be interpreted with caution. Because the measured spectral data are in raw sensor units, we apply a one-time calibration factor of 1.4, such that $r = 1.4r_m$, based on consistent results from four simulated and measured clear-sky spectra.

4.2 | A time series of spectral changes

Figure 11 shows how r varies in relation to multiple cloud shading and enhancement events of cumulus clouds on June 27 (FESSTVaL). The time series underlines that the fairly constant diffuse irradiance seen in the first case of cumulus is not representative of all cumulus passages, as most others show local distinctly enhanced diffuse irradiance. As for r , most noticeable are the large shifts ($\Delta r_m \approx 0.3$) towards blue-enriched light in fully shaded conditions, for example, at 0926 or 1013 UTC. Further away from transitions, for example, 0910 and 0950 UTC, there is enhanced irradiance, but no clear deviations from estimated clear-sky ratios. Interestingly, every shading event is flanked by brief reductions in r , typically 0.01–0.02 below r_{cs} , for example at 0919 and 0932 UTC, just as the Sun illuminates the local cloud edge as seen from the surface. Furthermore, it appears not every cloud enhancement has the same proportions of λ_s and λ_l , as there are different combinations of cloud enhancement magnitude and Δr_m (e.g., 0919 vs. 0932 UTC). This puts some value to the idea that the lack of extra local irradiance enhancement around shadows observed in the first case of Section 3 is due to counteracting local and nonlocal scattering sources. We speculate that the horizontal distribution of light scattered off (or escaping from, Várnai

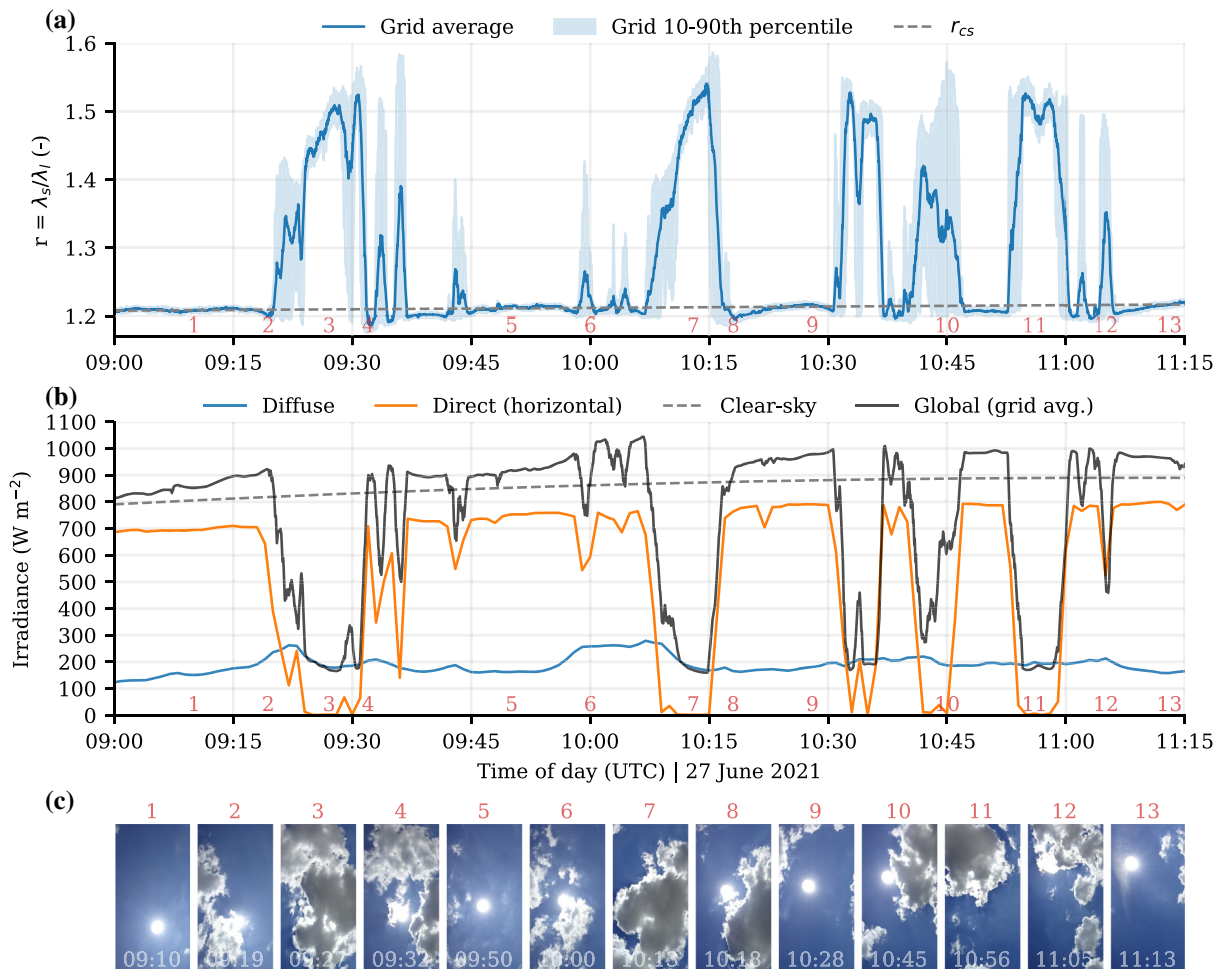


FIGURE 11 (a) Time series of r as measured by the network at FESSTVaL on June 27, 2021, (b) combined with broadband irradiance to illustrate the total effect of cloud passages. Direct and diffuse irradiance are 1-min averages of the Falkenberg suntracker, clear-sky is based on CAMS McClear. Global horizontal irradiance from 1-Hz data based on the mean values in the FROST network at Falkenberg. In (c), cropped images of one of the cloud cameras are shown for 13 manually chosen points in the time series to illustrate degrees of direct light obstruction of cumulus clouds. [Colour figure can be viewed at wileyonlinelibrary.com]

& Davies, 1999) cloud sides is approximately a clear-sky mix of diffuse and direct light ($r = r_{cs}$, $\Delta r_m = 0$) and acts over a larger area further away from the cloud(s), whereas localised forward scattering right at cloud edges is mostly direct light with lower r ($\Delta r_m \approx -0.01$ to -0.02). We will take a closer look at this phenomenon spatially using the cumulus, altocumulus, and cirrus cases of Section 3.

4.3 | Spatial patterns of spectral changes

Figure 12 shows Δr_m , now expressed in percentage points, for the cumulus, altocumulus, and cirrus cases previously described in Section 3. Data are plotted relative to r_{cs} , estimated partially from observations and simulations for the cumulus case or entirely from simulated spectra in the other two. The result is another diverse set of patterns,

albeit more noisy than for broadband irradiance due to reduced signal strength.

4.3.1 | Cumulus and mixing irradiance components

We first zoom in on four areas in the cumulus case (Figure 12a–c): 1051, 1056, 1101, and 1110 UTC. For the three enhanced areas, the shift in the middle one (1101 UTC) is about twice as strong ($\Delta r_m = -1.8\%$) compared with those before (1051 UTC, $\Delta r_m = -1.1\%$) and after (1110 UTC, $\Delta r_m = -0.8\%$), whereas the cloud enhancement in broadband irradiance only varies between 9% (1110 UTC) and 12% (1051 UTC). In the shadow at 1056 UTC, $\Delta r_m = 30.4\%$.

To help understand these numbers, we can hypothetically “mix” different amounts of clear-sky diffuse and

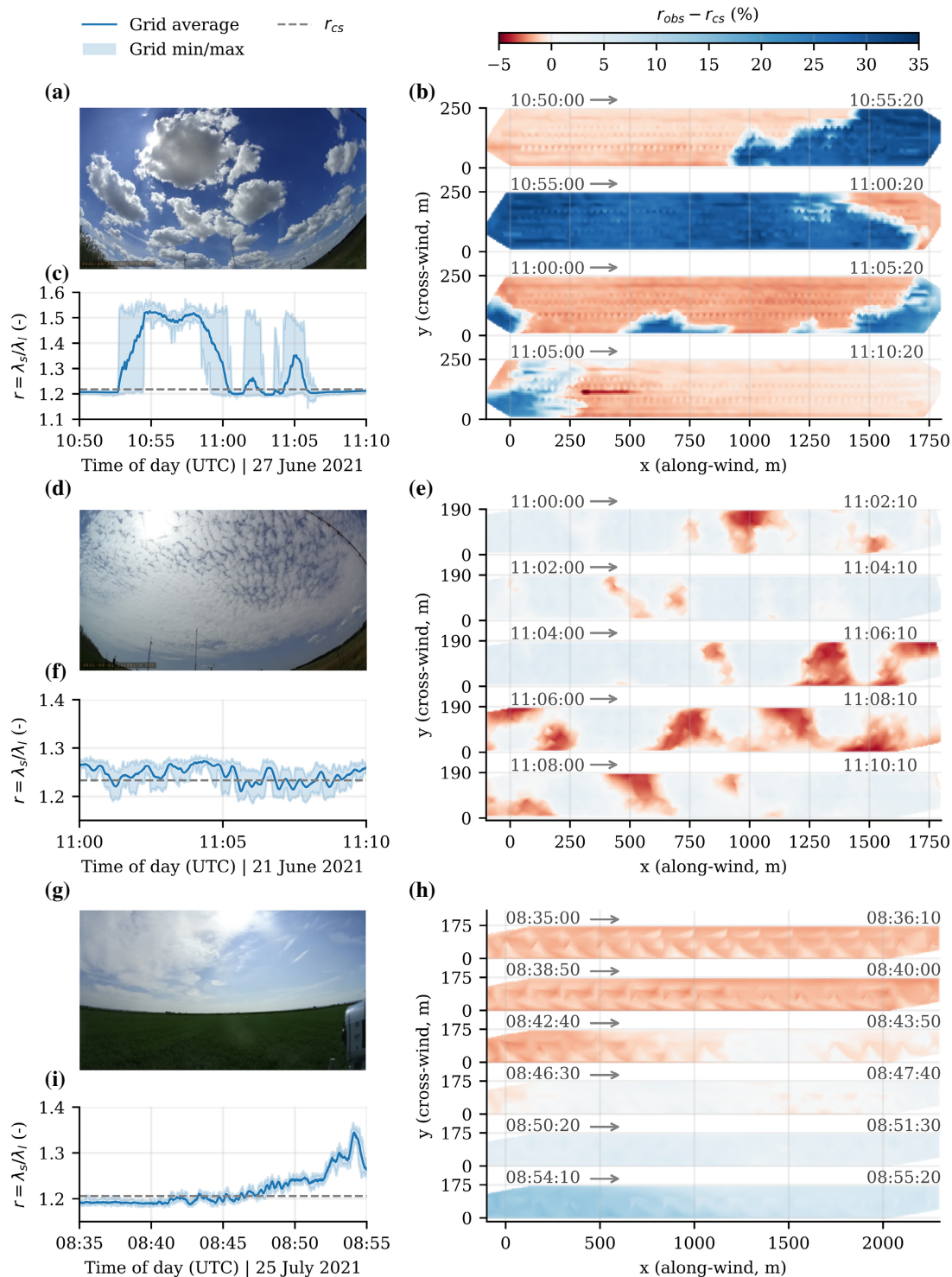


FIGURE 12 Spatial patterns of changes in r compared with clear-sky. Lower values indicate red enrichment, higher values blue enrichment. Values for r_{cs} are based on simulated clear-sky spectra. Note the asymmetric colour map scaling. Similar layout as Figure 10. [Colour figure can be viewed at [wileyonlinelibrary.com](https://onlinelibrary.wiley.com)]

direct irradiance together and calculate the resulting Δr_m . Assuming all $170 \text{ W}\cdot\text{m}^{-2}$ of irradiance in the shadow at 1056 UTC comes from a clear-sky diffuse source, Δr would be 74.7%. Adding $26 \text{ W}\cdot\text{m}^{-2}$ of clear-sky direct irradiance to the simulated $144 \text{ W}\cdot\text{m}^{-2}$ of clear-sky diffuse to match

the observed $170 \text{ W}\cdot\text{m}^{-2}$ of (non clear-sky) diffuse irradiance gives $\Delta r = 60.0\%$. If we first correct for a $\sim 25\%$ bias in the simulated clear-sky diffuse irradiance, based on observed clear-sky conditions at 0800 UTC, and then add enough clear-sky direct irradiance to match observed

values, we find $\Delta r = 45.0\%$. The first and last approximation are an under and over-estimation of the amount of blue-enriched irradiance in the shadow: the observed diffuse irradiance cannot be purely clear-sky diffuse given the presence of a scattering cloud field, nor would all of the enhanced diffuse irradiance relative to clear-sky originate from clear-sky direct irradiance alone. The middle estimate (60.0%) is nearly the same value as Δr_m if we apply the crosstalk correction γ (60.8%). It may be such a close match for the wrong reasons, but at least it represents a case where a significant portion of irradiance is coming from horizontally scattered direct or total irradiance mixed in with clear-sky diffuse.

Similarly, attributing all cloud enhancement to direct irradiance gives $\Delta r = -2.8\%$ and -2.5% for 1051 and 1110 UTC, an overestimation even after a γ correction, suggesting the extra irradiance is a mix of spectral irradiance closer to that of clear-sky conditions. For 1101 UTC, however, the estimate of $\Delta r = -2.7\%$ more closely matches the observed $\Delta r_m = -1.8\%$ (or $\gamma\Delta r_m \approx -3.6\%$) and coincides with a higher degree of fragmented semitransparent clouds that can effectively scatter direct irradiance forward. Alternatively, optically thick cumulus may also reduce r by blocking part of the diffuse clear-sky irradiance, though we expect this to be of secondary importance and more nonlocal due to the approximately isotropic nature of diffuse irradiance. Hygroscopic growth of aerosols in regions near cloud edges may also contribute to subtle changes in r and make the regions near cloud edges more potent in forward scattering.

Another cumulus case with notably lower cloud cover, higher cloud base, and high apparent haziness (June 17 at FESSTVaL, not shown) has qualitatively similar patterns around cloud shadows, but perturbations Δr_m are significantly larger. Thus, an analysis beyond two cumulus case studies and controlling for cloud and aerosol optical properties is necessary before drawing more general conclusions.

4.3.2 | Altocumulus and cirrus

The altocumulus (Figure 12d–f) and cirrus cases (Figure 12g–i) are more tricky to analyse, as here the clouds are all semitransparent and at higher altitude, thus making assumptions about the origin of light and its spectral signature more questionable. The relative spread in r_m is also larger in both, for altocumulus because the patterns are similar to the network scale and for the cirrus because it is earlier in the day with a weaker signal, visible in a noisier time series (Figure 12f) or pattern (Figure 12h). Values for Δr_m are nonetheless significantly

larger than the noise in both cases, and, although the hypothetical mixing of clear-sky spectra will not help to identify the scattering mechanisms, it can put the numbers in context.

For the darkest shadow in the altocumulus case, at 1104:15 UTC, $\Delta r_m = 3.8\%$. Assuming the increase of diffuse irradiance compared with clear-sky is all attributable to the clear-sky direct irradiance gives $\Delta r = 8.8\%$. This is an expected overestimation of blue enrichment (even after a factor γ), given that direct irradiance is $> 0 \text{ W}\cdot\text{m}^{-2}$. For one of the stronger cloud enhancements (30.0% at 1105:40), $\Delta r_m = -4.0\%$. Attributing all enhancement to direct irradiance gives $\Delta r = -4.0\%$, likely an underestimation given the transparency of the altocumulus to direct irradiance, suggesting part of the strongly enhanced diffuse irradiance may be more enriched in λ_1 . Averaged over the network, the differences between minima and maxima in r are small ($\approx 5\%$), about 6–7 times smaller than those of the cumulus case.

Lastly, for the cirrus case the cloud enhancement is 20.9% at 0839 UTC, with $\Delta r_m -1.5\%$. Assuming all enhancement is from clear-sky direct irradiance gives $\Delta r = -4.6\%$, resulting this time in a clear overestimation compared with what is measured. For the partially shaded area at 0850 UTC we find $\Delta r_m = 3.1\%$, and attributing the increase in observed diffuse to clear-sky direct irradiance gives $\Delta r = 6.3\% \approx \gamma\Delta r_m$. This matches, except it does not account for the fact that over half of the observed irradiance is of a direct origin (Figure 10g). The most optically thick part of the cirrus at 0854 UTC causes a significant shift towards shorter wavelengths as this contribution of direct irradiance reduces. Qualitative behaviour of cirrus, at least in this case, is thus the same: cloud enhancements are characterised by reductions in r , and (partial) shadings by increases. Variations in r for this cirrus case are in between those of the cumulus and altocumulus ($\approx 15\%$), with the spatiotemporal scale two orders of magnitude larger.

4.4 | Spectral patterns in summary

In all cases presented, both the cloud enhancement and shadow patterns show significant deviations from clear-sky spectral irradiance, which are particularly large in magnitude and spatiotemporal scale for the cumulus clouds. The fact that various combinations of diffuse and direct irradiance can create cloud enhancements of the same magnitude is well known (e.g., Gueymard, 2017), and so is the fact that clouds have spectral effects (e.g., O'Hirok et al., 2000). What we demonstrated in this section highlights that there are variations in part of the spectrum linked to where irradiance originates from, in a situation

where otherwise the optical properties, on the scale of these variations, are mostly wavelength-independent. In particular, the spectral signature of low and optically thick cumulus passages give some weight to our speculation that various light-scattering mechanisms affect different areas relative to the cloud.

5 | TEMPORAL PATTERNS DRIVEN BY WATER-VAPOUR VARIABILITY

One other significant spectral signature is that of water vapour. In this section, we will look at two examples of variability in atmospheric moisture as measured by the FROST network at FESSTVaL and LIAISE. These examples have a scope that is more towards regional scale (campaign area) land–atmosphere coupling and atmospheric dynamics under clear-sky conditions, rather than cloud-driven irradiance variability. The variations in water vapour are not large enough to affect broadband irradiance in the way clouds do, but they may help explain observed variations in GHI in clear-sky conditions.

5.1 | Deriving total column water vapour

Total column water vapour (TCWV) in the atmosphere is indirectly measurable using water-vapour absorption bands, where heightened levels of water vapour result in significantly reduced signal within absorption bands compared with other wavelengths. Figure 1 highlights two such bands for water, at 940 and 1130 nm. A strong absorption band is captured by the 940-nm channel of FROST, which in theory means we are able to detect changes in atmospheric moisture when comparing the 940-nm signal with a reference band outside the absorption band. Choosing a reference channel is limited by some sensor design and performance limitations. The cosine response varies between the three subgroups, such that changes in the ratio between two channels (e.g., 940 vs. 860 nm) are partially a result of instrument imperfections (see also Section 2.2) rather than changes in absorption strength. The choice of suitable channels is limited further by crosstalk at the shorter wavelengths of the subsensor for 940 nm, making the 900- and 940-nm channels the best options, despite 900 nm also partially being in a (weak) absorption band. Figure 13 illustrates the signal at 900 and 940 nm, where early in the day the ratio under clear-sky conditions is lower (more absorption) than noon due to the longer path length of irradiance. Shading from (semitransparent) cumuli also gives distinct absorption signals, though seemingly only for the most optically thick

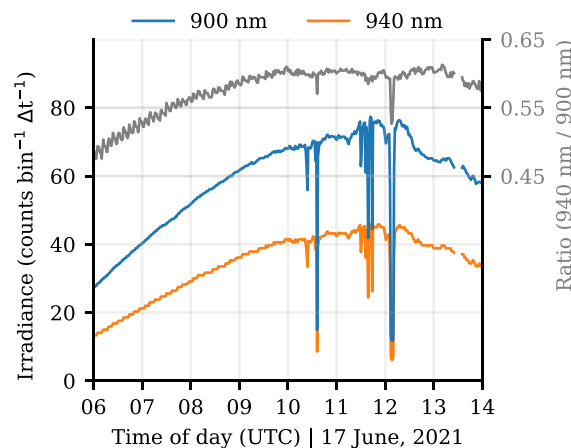


FIGURE 13 Spectral signature of water vapour measured by the 900- and 940-nm bands of FROST. The time series shows part of a daily cycle for a single sensor in the Falkenberg network, which is clear-sky until 1000 UTC, but features brief cumulus passages thereafter. The ratio of the 940/900 nm bands is shown in grey on the right axis. [Colour figure can be viewed at wileyonlinelibrary.com]

cumulus passages in this example. This might be due to the change in diffuse/direct partitioning, with a longer path length and thus absorption of diffuse irradiance, but any stronger statement requires a more careful analysis. But this underlines why only clear-sky conditions are suitable for estimating TCWV, as we currently cannot separate the effect of liquid water (or ice) from that of water vapour. One more limitation is the signal strength for the individual bands being low compared with the signal of water-vapour variations, even at high solar elevation angles. For a clear signal we therefore take a moving average of 120 s or more, thereby effectively reducing the temporal resolution. In a new version of FROST, the crosstalk and weak signal issues have been addressed (Heusinkveld et al., 2023).

In Figure 14a we show we can derive an absorption signal that is highly correlated to accurate reference measurements of TCWV. Higher values in the 940/900 nm ratio indicate less TCWV, so by flipping the y-axis this correlation ($r^2 = 0.75$) is more clearly visible. The reference TCWV measurement comes from a co-located microwave radiometer (Löhnert et al., 2022), with a 5-min moving average applied to both time series to get a comparable signal. The microwave radiometer measures along a single straight vertical path (Figure S7a), but the signal our sensors measure is a function of the path that light travels through the atmosphere, mostly from direct irradiance (Figure 2a). For fitting a model to the data we therefore include the atmospheric mass fraction (AMF), that is, the path length light travels through the atmosphere given a solar elevation angle α . This also means that the light our instruments measure has a horizontal footprint of

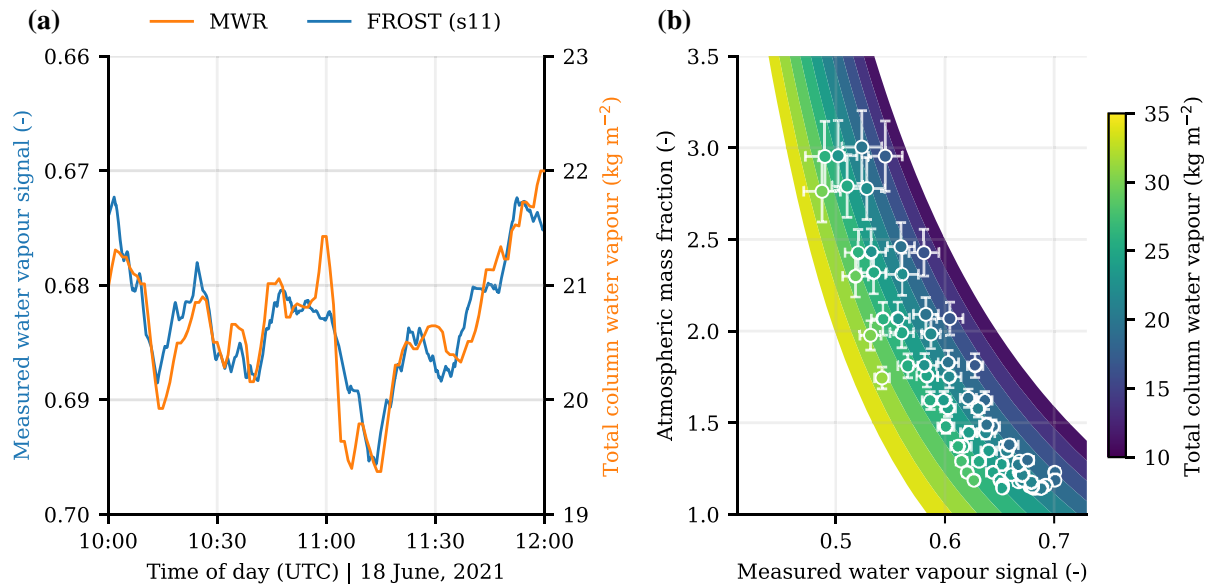


FIGURE 14 Total column water vapour (TCWV) derived from the radiometer water-vapour signal. In (a), an example time series of the signal (940/900 nm band ratio) compared with TCWV from the microwave radiometer (Löhnert et al., 2022) is shown for June 18 at Falkenberg (FESSTVaL). In (b), the scatters represent 30-min averages and standard deviations of the measured water-vapour signal and atmospheric mass fraction, coloured by the TCWV from the microwave radiometer. The results from the model best fit are shown in the curved shading. [Colour figure can be viewed at [wileyonlinelibrary.com](https://onlinelibrary.wiley.com)]

several kilometres, whereas the microwave radiometer is a vertical integral measurement at one fixed horizontal point. Furthermore, under clear-sky conditions, diffuse irradiance still typically constitutes about 10%–30% of GHI (see Figure S1) and would have travelled a longer distance through the atmosphere (by definition, as it is scattered light compared with direct light). This effect is taken into account implicitly, as the diffuse fraction is also a function of solar elevation angle and thus the atmospheric mass fraction. We expect some bias in our model fit for extremely clear or hazy days, but we have no clear signal or quantification of its effect within our observational dataset.

The relationship between TCWV, AMF, and measured water-vapour absorption (WVA) is captured by a function of the form $f(x, y) = ax + b + cy^2 + dy + exy$, where $x = \text{WVA}$ and $y = \text{AMF}$. Figure 14b illustrates the best fit of this model, based on 30-min averages of all available clear-sky data during FESSTVaL for sensor 11 at Falkenberg compared with the microwave radiometer. Measurement uncertainties are based on the standard deviation within the 30-min windows.

Since there is a limitation to the accuracy of the spectra from sensor to sensor and within sensors (Section 2.2), we find no gain by training the model from data of all sensors together, or calibrating sensors individually as we do for GHI, likely to due overfitting. Instead, we apply the best fit based on sensor 11 at FESSTVaL and use the

uncertainty in the ratio between spectral bands as an error estimation. Similar to broadband irradiance estimates, one could fine-tune the calibration on a case-specific basis if a high-quality reference is available. We estimate uncertainty by taking the standard deviation between all sensors in a network, which results in $\pm 0.5 \text{ kg}\cdot\text{m}^{-2}$ for sufficiently high solar elevation angles ($\alpha > 30^\circ$) and increases towards sunset and sunrise.

5.2 | Sub-mesoscale water-vapour variability at FESSTVaL

June 18 at FESSTVaL was a clear-sky, warm summer day (maximum 2-m temperature of 31°C). There are intra-hourly variations in TCWV of $1\text{--}3 \text{ kg}\cdot\text{m}^{-2}$, as illustrated in Figure 15 for various locations within the larger campaign area (Figure 3b). With a predominantly southerly wind of $\approx 9 \text{ m}\cdot\text{s}^{-1}$ average over the lower troposphere, we tried to track moisture patterns across a 10-km south–north transect in the FESSTVaL domain (Figure 3b), south of Falkenberg to Lindenberg, at 10- and 20-min time-lags respectively. The southern and Falkenberg measurements are based on the TCWV derived from our instruments, with two high-quality measurements taken from the microwave radiometers at Falkenberg and Lindenberg. While our instruments and the microwave radiometers at Falkenberg are in agreement on the local variations (despite a bias of $\sim 0.5 \text{ kg}\cdot\text{m}^{-2}$), there appears to be no

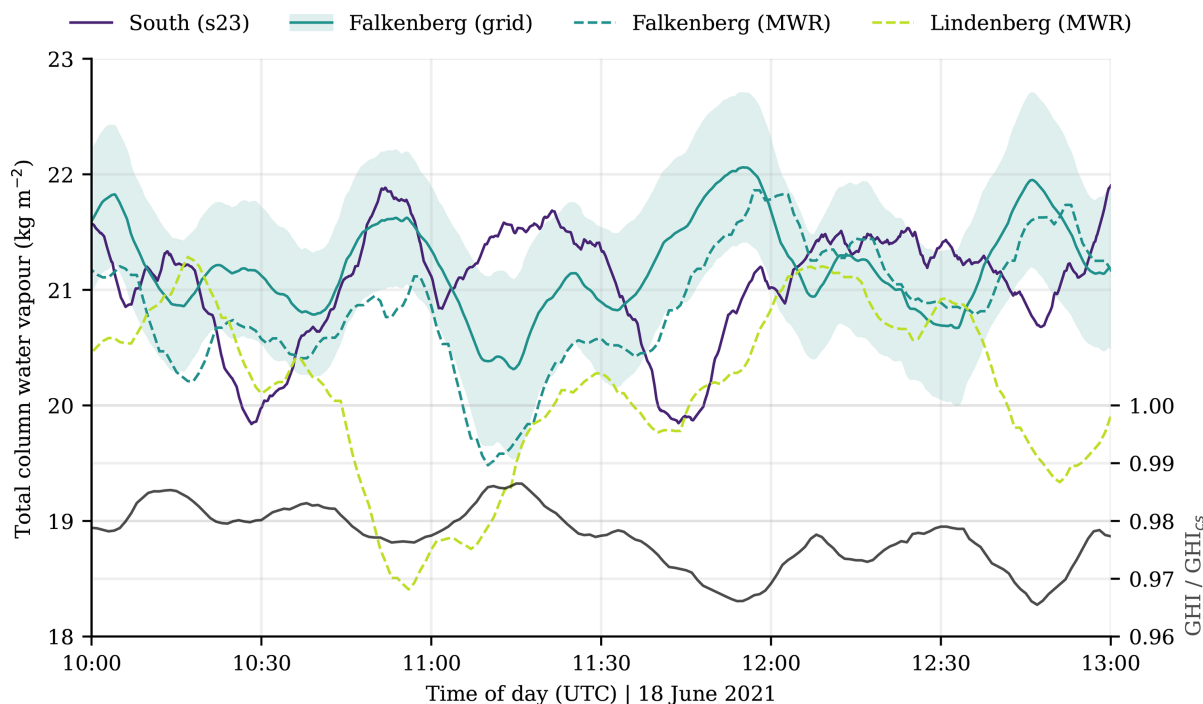


FIGURE 15 Time series of total column water vapour (TCWV) from a south to north transect in the FESSTVaL campaign area. FROST-derived TCWV is compared with high-quality microwave radiometer measurements, both resampled to 10-min moving averages. The shading is the FROST grid standard deviation. The south to north transect (south–Falkenberg–Lindenberg) is approximately 10 km, with Falkenberg in the middle (see also Figure 3b), and the wind is $\approx 10 \text{ m s}^{-1}$ from the south. The black line is the Falkenberg global horizontal irradiance relative to clear-sky, also with a 10-min moving average. [Colour figure can be viewed at [wileyonlinelibrary.com](https://onlinelibrary.wiley.com)]

correlation between the southern (s23) and northern (Lindenberg) location (Figure 15). We therefore think that the temporal variability in TCWV is driven more locally by turbulence structures in the convective boundary layer, rather than the advection of (sub)mesoscale horizontal patterns in moisture. In support of this, observed variations in GHI relative to clear-sky at Falkenberg show an anticorrelation with TCWV ($r = -0.79$), where $+1 \text{ mm TCWV} \approx -1\% \text{ GHI}$ (Figure 15). These changes in GHI cannot be explained by the direct effect of TCWV variations alone, which would be closer to $-0.1\% \text{ GHI}$ for $+1 \text{ mm}$ of water vapour, and might instead point to buoyant plumes in the boundary layer that carry extra aerosols from the surface. The more subtle differences in variability between FROST and microwave radiometer based measurements may be explained by the different footprint of FROST sampling different moisture structures, given its horizontal component in the diagonal cross-section through the atmosphere (Figure 2a).

5.3 | Variability in water vapour at LIAISE

During the LIAISE campaign, most days were clear-sky (Figure 4), which gives ample data to study intraday

variability in atmospheric moisture. The campaign area is characterized by complex meteorology due to a combination of topography, strong heterogeneity in surface fluxes at various scales due to irrigation (Bowen ratio between 0.01 and 30, Mangan et al. (2023)), and late afternoon southeastern sea-breeze dynamics with varying timing and strength. This collection of complex factors affecting local weather is not captured by high-resolution weather models, and even less so by the one ERA5 grid cell covering the campaign area. Measuring TCWV helps to identify internal boundary layers and moisture plumes at the local scale to synoptic-scale advection, which are features that contribute to moisture variability. We apply the best fit derived from FESSTVaL (Figure 14) to the sensor network at the irrigated La Cendrosa site. Figure 16 shows the resulting time series for four (clear-sky) IOP days compared with ERA5 and hourly radiosondes, using a 3-min moving average to get a clear signal. FROST-derived TCWV time series and soundings do not agree at all with the magnitude and trends of ERA5, which highlights the difficulty (coarse) models have with the complex meteorology in the LIAISE domain. Radiosondes and our spectrally derived TCWV time series are in much better agreement overall, and provide a good validation of our calibration methodology. Derivation of TCWV

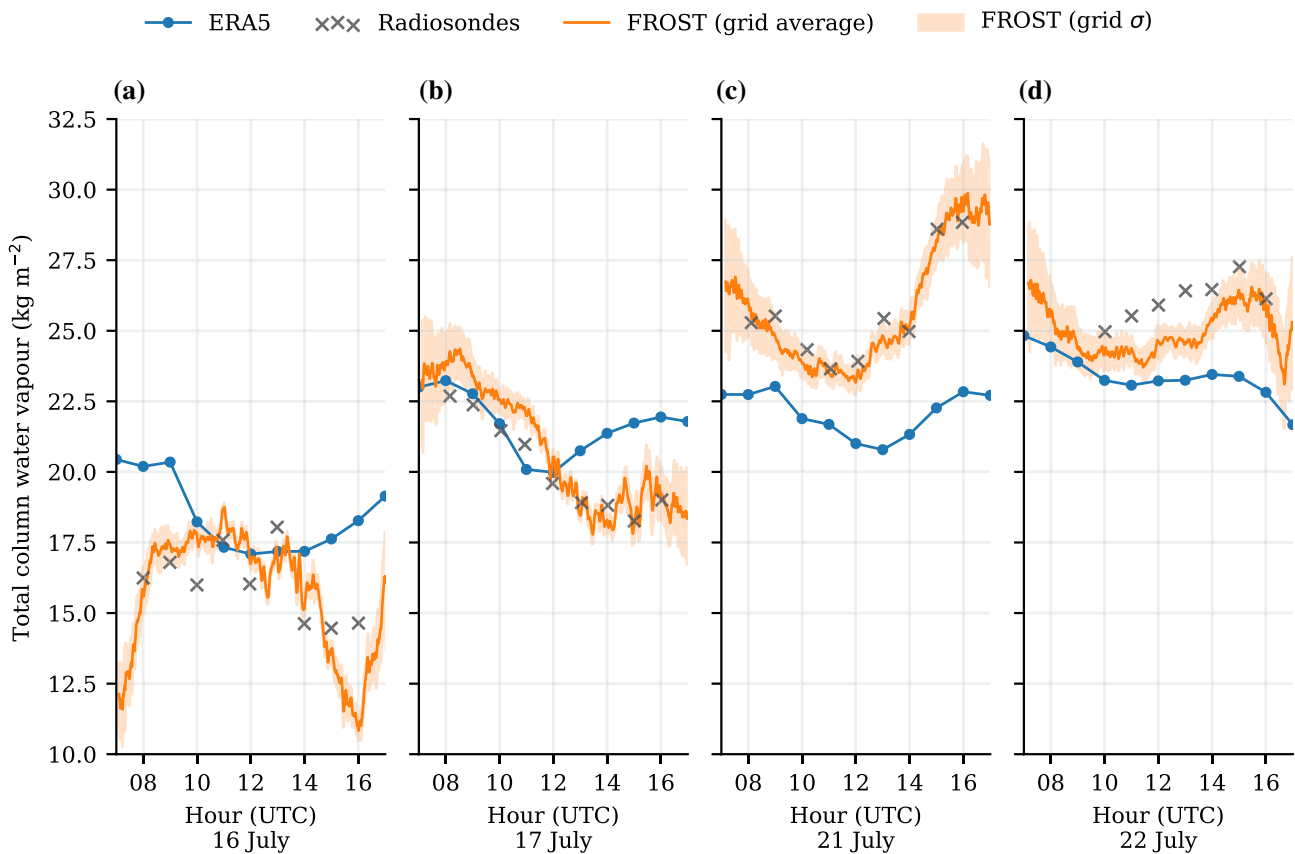


FIGURE 16 Time series of total column water vapour (TCWV) at La Cendrosa during LIAISE. Irradiance based measurements are compared with ERA5 (interpolated to La Cendrosa) and hourly soundings of La Cendrosa combined with Els Plans. The uncertainty range of the FROST measurements is the standard deviation among sensors in the network. The four dates are ideal clear-sky days and official Intensive Observation Periods. [Colour figure can be viewed at wileyonlinelibrary.com]

from radiosondes is precarious, though, since the hourly boundary-layer radiosondes at La Cendrosa (Price, 2023) only reach to about 1.5–4 km and need to be supplemented with hourly tropospheric radiosondes from Els Plans (Canut & Garroute, 2022), a nonirrigated location 14.1 km to the southeast. The atmospheric conditions in Els Plans and La Cendrosa converge above their respective local boundary layers to a regional atmospheric profile, described by a blending height of approximately 1.5 km (Mangan et al., 2023). For each sounding in La Cendrosa, we supplement its information with the mid-to upper-tropospheric data gathered from the closest (in time) Els Plans sounding (schematically illustrated in Figure S7b). Timing and footprint differences between instantaneous spectrum-derived TCWV and hourly combined soundings are, we believe, the main reason for differences between their measurements.

In terms of variability, there seem to be multiple time scales at play. On hourly time-scales, trends in TCWV can be up to $5 \text{ kg} \cdot \text{m}^{-2} \cdot \text{h}^{-1}$, whereas on minute time-scales the constant fluctuations do not exceed $1 \text{ kg} \cdot \text{m}^{-2}$. The latter we believe to be driven by moist boundary-layer

thermals and subsequent dry air entrainment. Daily cycles of boundary-layer drying through local advection (Mangan et al., 2023) and synoptic-scale advection of air masses (captured by ERA5) explain the multihour and day-to-day variations respectively.

To explain the subhourly variability in water vapour, we correlate variability of measured specific humidity at 45 m (q_{45m}) in the well-mixed boundary layer to variation in TCWV. Both time series are resampled to a common resolution of 2 min, the lowest we can reach with our TCWV measurements for a usable signal-to-noise ratio. To exclude hourly or daily trends, we define variations in TCWV or q_{45m} as the deviations with respect to their 60-min centred moving average. The boundary layer contains a significant portion of the total vertical moisture, but we find the resulting correlation between variations in q_{45m} and the TCWV to be very weak, with an r^2 of 0.17. Rather, the TCWV from FROST has larger scale variations due to its diagonal cross-sectional footprint through turbulence structures in the whole boundary layer, compared with a single-point measurement close to the surface. For an illustration of this difference and the poor

correlation between the two time series, please refer to Figure S8.

In summary, we find FROST is able to capture moisture variability that is representative for the kilometre scale and above, rather than at individual field level. In a newer version of FROST, we have an improved the signal-to-noise ratio and thus require shorter time-averaging, which may enable the ability to capture variations on shorter time-scales than 2 min. This could offer a flexible, low-cost alternative to a microwave radiometer or soundings, if absolute accuracy is of lesser importance.

6 | CONCLUSIONS AND OUTLOOK

Using low-cost radiometers calibrated against high-quality reference stations, we have gathered two high-resolution and spectrally resolved datasets of surface solar irradiance at cloud-scale. In combination with supplementary observations and simulations, such as cloud cameras at FESSTVaL, soundings at LIAISE, and simulated clear-sky spectra, we have derived insights into spatial patterns of surface irradiance caused by three types of cloud and by cloud-free atmospheric moisture variability. This work demonstrates how low-cost instruments can provide accurate and detailed spatial measurements, making them an effective addition to field campaigns. This is especially the case for campaigns in areas where deployment of expensive, heavy, and high-maintenance equipment is difficult.

We have analysed cases of boundary-layer cumulus, mid-level altocumulus, and high-level cirrus. All three of the cases have distinctly different surface irradiance patterns, spatial scales of variability (50 m to 30 km), cloud types, direct/diffuse partitioning, spectral irradiance, and mechanisms through which these patterns are formed. The contribution of individual scattering mechanisms to the total variability remains difficult to quantify, due to the complexity of real-world measurements. However, by comparing changes between visible blue and red wavelengths, we think the enhanced irradiance next to the shadow of a cumulus has a large contribution of forward-scattered light from the local cloud edge. This contrasts with the situation further away from a shadow, where the enhanced radiation originates mostly from the sides of cloud in the overall cloud field. For mid- and high-level cloud cases, conditions of reduced irradiance are more blue and enhanced irradiance more red compared with clear-sky, similar to cumulus. However, the cause of changes in spectral irradiance in these cases is inconclusive in our analysis. The calculations we perform to explain the changes do not match the

observations quantitatively, probably because the assumptions underlying this method break down for higher altitude clouds.

None of the three commonly occurring cases we have discussed is well represented by state-of-the-art numerical weather prediction, nor by most cloud-resolving models in academic setups, due to simplifications in the radiative transfer calculations. In particular, altocumulus appears to be potent in creating strong, localised peaks, and may be underrepresented in the field of 3D radiative transfer research. We have only focused on cloud cases that occur in isolation, to make interpretation easier, but often clouds of varying type occur simultaneously and the effects may not be simply additive. This proves a real challenge in both observational and modelling studies.

We are also able to capture variability in the irradiance spectrum that arises from significant changes in atmospheric water vapour in clear-sky conditions, despite some limitations on sensor quality for spectral irradiance. These local variations are often larger than synoptic-scale moisture advection, but correlate with variations in GHI of the order of one per cent, and thus illustrate heterogeneity in moisture fluxes and optical properties of a cloud-free boundary layer.

The datasets presented provide observations of cloud- and moisture-driven irradiance variability that can guide the development of radiative transfer variability parameterisations. The datasets can furthermore help constrain the input for land-surface, photosynthesis, or dynamic vegetation models that are currently driven by incorrect (spectral) irradiance distributions. A more comprehensive understanding of cloud-driven irradiance variability will, however, require analyses of many more clouds and irradiance patterns in datasets such as these. We believe the analyses of complex real-world data can be improved by using idealised cloud-resolving models with 3D radiative transfer to characterise mechanisms quantitatively.

ACKNOWLEDGEMENTS

Our thanks goes out to the FESSTVaL and LIAISE campaign organisers and host institutes for enabling us to gather observations alongside many others, without which this work would not have been possible. W. Mol, B. Heusinkveld, M. Veerman, and C. van Heerwaarden acknowledge funding from the Dutch Research Council (Nederlandse Organisatie voor Wetenschappelijk Onderzoek) (grant: VI.Vidi.192.068).

DATA AVAILABILITY STATEMENT

All data in this publication are open-access.

All data measured with FROST sensors at FESSTVaL and LIAISE are published open-access datasets. These

include ready-to-use calibrated quality-controlled data and the raw instrument data, which require pyranometer calibration references:

- Radiometer data FESSTVaL (Mol, Heusinkveld, & van Heerwaarden, 2023a): <https://doi.org/10.25592/uhhfdm.10272>,
- Radiometer data LIAISE (Mol, Heusinkveld, & Van Heerwaarden, 2023b): <https://doi.org/10.5281/zenodo.7966437>.

The code for calibration of raw data and analyses presented in this work, the video of Section 3.2, and the libRadtran input files are available at <https://zenodo.org/records/10159129>. La Cendrosa solar irradiance is not yet available at the time of writing, but will be available on the LIAISE database: <https://liaise.aeris-data.fr/page-catalogue/?uuiid=d9608a55-b836-427b-a186-e007462012b9>.

ENDNOTES

¹<https://liaise.aeris-data.fr/>.

²See <https://fesstval.de> and Hohenegger et al. (2023) for details.

³<https://liaise.aeris-data.fr/>.

ORCID

Wouter Mol  <https://orcid.org/0000-0003-0133-0995>

Bert Heusinkveld  <https://orcid.org/0000-0001-7844-8989>

Mary Rose Mangan  <https://orcid.org/0000-0002-9017-7939>

Oscar Hartogensis  <https://orcid.org/0000-0001-8920-9975>

Menno Veerman  <https://orcid.org/0000-0002-4869-3948>

Chiel van Heerwaarden  <https://orcid.org/0000-0001-7202-3525>

REFERENCES

- Ackerman, S.A. & Stephens, G.L. (1987) The absorption of solar radiation by cloud droplets: an application of anomalous diffraction theory. *Journal of the Atmospheric Sciences*, 44(12), 1574–1588. Available from: [https://doi.org/10.1175/1520-0469\(1987\)044\(1574:TAOSRB\)2.0.CO;2](https://doi.org/10.1175/1520-0469(1987)044(1574:TAOSRB)2.0.CO;2)
- Canut, G. & Garrouste, O. (2022) LIAISE_LA-CENDROSA_CNRM_RS_L2. [Data set] Aeris. <https://doi.org/10.25326/322>
- Cordero, R.R., Feron, S., Damiani, A., Sepúlveda, E., Jorquera, J., Redondas, A. et al. (2023) Surface solar extremes in the most irradiated region on earth, altiplano. *Bulletin of the American Meteorological Society*, 104(6), E1206–E1221. Available from: <https://doi.org/10.1175/BAMS-D-22-0215.1>
- Dirnberger, D., Blackburn, G., Müller, B. & Reise, C. (2015) On the impact of solar spectral irradiance on the yield of different PV technologies. *Solar Energy Materials and Solar Cells*, 132, 431–442. Available from: <https://doi.org/10.1016/j.solmat.2014.09.034>
- Driemel, A., Augustine, J., Behrens, K., Colle, S., Cox, C., Cuevas-Agulló, E. et al. (2018) Baseline surface radiation network (BSRN): structure and data description (1992–2017). *Earth System Science Data*, 10(3), 1491–1501. Available from: <https://doi.org/10.5194/essd-10-1491-2018>
- Durand, M., Murchie, E.H., Lindfors, A.V., Urban, O., Aphalo, P.J. & Robson, T.M. (2021) Diffuse solar radiation and canopy photosynthesis in a changing environment. *Agricultural and Forest Meteorology*, 311, 108684. Available from: <https://doi.org/10.1016/j.agrformet.2021.108684>
- Emde, C., Buras-Schnell, R., Kylling, A., Mayer, B., Gasteiger, J., Hamann, U. et al. (2016) The libRadtran software package for radiative transfer calculations (version 2.0.1). *Geoscientific Model Development*, 9(5), 1647–1672. Available from: <https://doi.org/10.5194/gmd-9-1647-2016>
- Gristey, J.J., Feingold, G., Schmidt, K.S. & Chen, H. (2022) Influence of aerosol embedded in shallow cumulus cloud fields on the surface solar irradiance. *Journal of Geophysical Research: Atmospheres*, 127(11), e2022JD036822. Available from: <https://doi.org/10.1029/2022JD036822>
- Gschwind, B., Wald, L., Blanc, P., Lefèvre, M., Schroedter-Homscheidt, M. & Arola, A. (2019) Improving the McClear model estimating the downwelling solar radiation at ground level in cloud-free conditions – McClear-v3. *metz*, 28(2), 147–163. Available from: <https://doi.org/10.1127/metz/2019/0946>
- Gueymard, C.A. (2017) Cloud and albedo enhancement impacts on solar irradiance using high-frequency measurements from thermopile and photodiode radiometers. Part 1: impacts on global horizontal irradiance. *Solar Energy*, 153, 755–765. Available from: <https://doi.org/10.1016/j.solener.2017.05.004>
- Heusinkveld, B.G., Mol, W.B. & van Heerwaarden, C.C. (2023) A new accurate low-cost instrument for fast synchronized spatial measurements of light spectra. *Atmospheric Measurement Techniques*, 16(15), 3767–3785. Available from: <https://doi.org/10.5194/amt-16-3767-2023>
- Hogan, R.J. & Bozzo, A. (2018) A Flexible and Efficient Radiation Scheme for the ECMWF Model. *Journal of Advances in Modeling Earth Systems*, 10(8), 1990–2008. Available from: <https://doi.org/10.1029/2018MS001364>
- Hohenegger, C., Ament, F., Beyrich, F., Löhnert, U., Rust, H., Bange, J. et al. (2023) FESSTVaL: the field experiment on submesoscale spatio-temporal variability in lindenbergl. *Bulletin of the American Meteorological Society*, 104(10), E1875–E1892. Available from: <https://doi.org/10.1175/BAMS-D-21-0330.1>
- Jakub, F. & Mayer, B. (2017) The role of 1-D and 3-D radiative heating in the organization of shallow cumulus convection and the formation of cloud streets. *Atmospheric Chemistry and Physics*, 17(21), 13317–13327. Available from: <https://doi.org/10.5194/acp-17-13317-2017>
- Key, J.R., Yang, P., Baum, B.A. & Nasiri, S.L. (2002) Parameterization of shortwave ice cloud optical properties for various particle habits. *Journal of Geophysical Research: Atmospheres*, 107(D13), AAC 7–1–AAC 7–10. Available from: <https://doi.org/10.1029/2001JD000742>

- Kipp & Zonen. (2004) CM22 precision pyranometer instruction manual. <https://www.kippzonen.com/Download/55/CM-22-Pyranometer-Manual>
- Kirsch, B., Hohenegger, C., Klocke, D., Senke, R., Offermann, M. & Ament, F. (2022) Sub-mesoscale observations of convective cold pools with a dense station network in Hamburg, Germany. *Earth System Science Data*, 14(8), 3531–3548. Available from: <https://doi.org/10.5194/essd-14-3531-2022>
- Kreuwel, F.P.M., Mol, W.B., Vilà-Guerau de Arellano, J. & van Heerwaarden, C.C. (2021) Characterizing solar PV grid overvoltages by data blending advanced metering infrastructure with meteorology. *Solar Energy*, 227, 312–320. Available from: <https://doi.org/10.1016/j.solener.2021.09.009>
- Liang, X. (2017) Emerging power quality challenges due to integration of renewable energy sources. *IEEE Transactions on Industry Applications*, 53(2), 855–866. Available from: <https://doi.org/10.1109/TIA.2016.2626253>
- Lohmann, G.M., Monahan, A.H. & Heinemann, D. (2016) Local short-term variability in solar irradiance. *Atmospheric Chemistry and Physics*, 16(10), 6365–6379. Available from: <https://doi.org/10.5194/acp-16-6365-2016>
- Löhnert, U., Knist, C., Böck, T. & Pospichal, B. (2022) Microwave radiometer observations during FESSTVaL 2021 (Version 00) [Data set]. Universität Hamburg. <https://doi.org/10.25592/UHHFDM.10198>
- Lohou, F. & Patton, E.G. (2014) Surface energy balance and buoyancy response to shallow cumulus shading. *Journal of the Atmospheric Sciences*, 71(2), 665–682. Available from: <https://doi.org/10.1175/JAS-D-13-0145.1>
- Madhavan, B.L., Deneke, H., Witthuhn, J. & Macke, A. (2017) Multi-resolution analysis of the spatiotemporal variability in global radiation observed by a dense network of 99 pyranometers. *Atmospheric Chemistry and Physics*, 17(5), 3317–3338. Available from: <https://doi.org/10.5194/acp-17-3317-2017>
- Madhavan, B.L., Kalisch, J. & Macke, A. (2016) Shortwave surface radiation network for observing small-scale cloud inhomogeneity fields. *Atmospheric Measurement Techniques*, 9(3), 1153–1166. Available from: <https://doi.org/10.5194/amt-9-1153-2016>
- Mangan, M.R., Hartogensis, O., Boone, A., Branch, O., Canut, G., Cuxart, J. et al. (2023) The surface-boundary layer connection across spatial scales of irrigation-driven thermal heterogeneity: an integrated data and modeling study of the LIAISE field campaign. *Agricultural and Forest Meteorology*, 335, 109452. Available from: <https://doi.org/10.1016/j.agrformet.2023.109452>
- Mol, W., Heusinkveld, B. & van Heerwaarden, C. (2023a) Radiometer grid at falkenberg and surroundings, downwelling shortwave radiation, fesstval campaign. <https://doi.org/10.25592/uhhfdm.12548>
- Mol, W., Heusinkveld, B. & Van Heerwaarden, C. (2023b) Radiometer network dataset of 10 hz spectral irradiance and derived variables (liaise campaign). <https://doi.org/10.5281/ZENODO.7966437>
- Mol, W.B., van Stratum, B.J.H., Knap, W.H. & van Heerwaarden, C.C. (2023) Reconciling observations of solar irradiance variability with cloud size distributions. *Journal of Geophysical Research: Atmospheres*, 128(5), e2022JD037894. Available from: <https://doi.org/10.1029/2022JD037894>
- O'Hirok, W. & Gautier, C. (1998) A three-dimensional radiative transfer model to investigate the solar radiation within a cloudy atmosphere. Part II: spectral effects. *Journal of the Atmospheric Sciences*, 55(19), 3065–3076. Available from: [https://doi.org/10.1175/1520-0469\(1998\)055<3065:ATDRTM>2.0.CO;2](https://doi.org/10.1175/1520-0469(1998)055<3065:ATDRTM>2.0.CO;2)
- O'Hirok, W., Gautier, C. & Ricchiazzi, P. (2000) Spectral signature of column solar radiation absorption during the atmospheric radiation measurement enhanced shortwave experiment (ARESE). *Journal of Geophysical Research: Atmospheres*, 105(D13), 17471–17480. Available from: <https://doi.org/10.1029/2000JD900190>
- Pincus, R. & Evans, K.F. (2009) Computational cost and accuracy in calculating three-dimensional radiative transfer: results for new implementations of Monte Carlo and SHDOM. *Journal of the Atmospheric Sciences*, 66(10), 3131–3146. Available from: <https://doi.org/10.1175/2009JAS3137.1>
- Pingswept. (2022) Pysolar is a collection of Python libraries for simulating the irradiation of any point on earth by the sun. <https://github.com/pingswept/pysolar>
- Price, J. (2023) LIAISE_ELS-PLANS_UKMO_radiosondes_L1. [Data set] AERIS. <https://doi.org/10.25326/429>
- Romps, D.M., Öktem, R., Endo, S. & Vogelmann, A.M. (2021) On the life cycle of a shallow cumulus cloud: Is it a bubble or plume, active or forced? *Journal of the Atmospheric Sciences*, 78(9), 2823–2833. Available from: <https://doi.org/10.1175/JAS-D-20-0361.1>
- Sassen, K. & Wang, Z. (2008) Classifying clouds around the globe with the CloudSat radar: 1-year of results. *Geophysical Research Letters*, 35(4). Available from: <https://doi.org/10.1029/2007GL032591>
- Schade, N.H., Macke, A., Sandmann, H. & Stick, C. (2007) Enhanced solar global irradiance during cloudy sky conditions. *Meteorologische Zeitschrift*, 16(3), 295–303. Available from: <https://doi.org/10.1127/0941-2948/2007/0206>
- Schäfer, S.A.K., Hogan, R.J., Klinger, C., Chiu, J.C. & Mayer, B. (2016) Representing 3-D cloud radiation effects in two-stream schemes: 1. Longwave considerations and effective cloud edge length. *Journal of Geophysical Research: Atmospheres*, 121(14), 8567–8582. Available from: <https://doi.org/10.1002/2016JD024876>
- Schmidt, K.S., Pilewskie, P., Mayer, B., Wendisch, M., Kindel, B., Platnick, S. et al. (2010) Apparent absorption of solar spectral irradiance in heterogeneous ice clouds. *Journal of Geophysical Research: Atmospheres*, 115(D10). Available from: <https://doi.org/10.1029/2009JD013124>
- Tabar, M.R.R., Anvari, M., Lohmann, G., Heinemann, D., Wächter, M., Milan, P. et al. (2014) Kolmogorov spectrum of renewable wind and solar power fluctuations. *European Physical Journal Special Topics*, 223(12), 2637–2644. Available from: <https://doi.org/10.1140/epjst/e2014-02217-8>
- Tomson, T. (2010) Fast dynamic processes of solar radiation. *Solar Energy*, 84(2), 318–323. Available from: <https://doi.org/10.1016/j.solener.2009.11.013>
- Ukkonen, P. & Hogan, R. J. (2024) Twelve times faster yet accurate: A new state-of-the-art in radiation schemes via performance and spectral optimization. *Journal of Advances in Modeling Earth Systems*, 16(1). Portico. <https://doi.org/10.1029/2023ms003932>
- Várnai, T. & Davies, R. (1999) Effects of cloud heterogeneities on shortwave radiation: comparison of cloud-top variability and internal heterogeneity. *Journal of the Atmospheric Sciences*, 56(24), 4206–4224. Available from: [https://doi.org/10.1175/1520-0469\(1999\)056<4206:EOCHOS>2.0.CO;2](https://doi.org/10.1175/1520-0469(1999)056<4206:EOCHOS>2.0.CO;2)

- Veerman, M.A., van Stratum, B.J.H. & van Heerwaarden, C.C. (2022) A case study of cumulus convection over land in cloud-resolving simulations with a coupled ray tracer. *Geophysical Research Letters*, e2022GL100808. Available from: <https://doi.org/10.1029/2022GL100808>
- Villefranque, N., Barker, H.W., Cole, J.N.S. & Qu, Z. (2023) A functionalized monte carlo 3D radiative transfer model: radiative effects of clouds over reflecting surfaces. *Journal of Advances in Modeling Earth Systems*, 15(7), e2023MS003674. Available from: <https://doi.org/10.1029/2023MS003674>
- Weigl, T., Nagl, L., Weizenbeck, J., Zehner, M., Augel, M., Ochsner, P. et al. (2012) Modelling and validation of spatial irradiance characteristics for localised irradiance fluctuations and enhancements. In: *Proceedings of the 27th Photovoltaic Solar Energy Conference*, Frankfurt. https://www.researchgate.net/publication/237353116_Modelling_and_Validation_of_Spatial_Irradiance_Characteristics_for_Localised_Irradiance_Fluctuations_and_Enhancements
- Wood, R. & Field, P.R. (2011) The distribution of cloud horizontal sizes. *Journal of Climate*, 24(18), 4800–4816. Available from: <https://doi.org/10.1175/2011JCLI4056.1>
- Yang, D., Wang, W., Gueymard, C.A., Hong, T., Kleissl, J., Huang, J. et al. (2022) A review of solar forecasting, its dependence on atmospheric sciences and implications for grid integration: towards carbon neutrality. *Renewable and Sustainable Energy Reviews*, 161, 112348. Available from: <https://doi.org/10.1016/j.rser.2022.112348>
- Yordanov, G.H., Saetre, T.O. & Midtgård, O. (2013) 100-millisecond resolution for accurate overirradiance measurements. *IEEE Journal of Photovoltaics*, 3(4), 1354–1360. Available from: <https://doi.org/10.1109/JPHOTOV.2013.2264621>
- Yordanov, G.H., Saetre, T.O. & Midtgård, O.-M. (2015) Extreme overirradiance events in Norway: 1.6 suns measured close to 60°N. *Solar Energy*, 115, 68–73. Available from: <https://doi.org/10.1016/j.solener.2015.02.020>

SUPPORTING INFORMATION

Additional supporting information can be found online in the Supporting Information section at the end of this article.

How to cite this article: Mol, W., Heusinkveld, B., Mangan, M.R., Hartogensis, O., Veerman, M. & van Heerwaarden, C. (2024) Observed patterns of surface solar irradiance under cloudy and clear-sky conditions. *Quarterly Journal of the Royal Meteorological Society*, 1–26. Available from: <https://doi.org/10.1002/qj.4712>